

# Differences between CO- and calcium triplet-derived velocity dispersions in spiral galaxies: evidence for central star formation?

Rogemar A. Riffel<sup>1\*</sup>, Luis C. Ho<sup>2,3</sup>, Rachel Mason<sup>4</sup>, Alberto Rodríguez-Ardila<sup>5</sup>  
Lucimara Martins<sup>6</sup>, Rogério Riffel<sup>7</sup>, Ruben Diaz<sup>8</sup>, Luis Colina<sup>9</sup>,  
Almudena Alonso-Herrero<sup>10</sup>, Helene Flohic<sup>11</sup>, Omaira Gonzalez Martin<sup>12,13</sup>,  
Paulina Lira<sup>14</sup>, Richard McDermid<sup>4,15</sup>, Cristina Ramos Almeida<sup>12,13</sup>,  
Ricardo Schiavon<sup>2,16</sup>, Karun Thanjavur<sup>17</sup>, Daniel Ruschel Dutra<sup>7,12</sup>,  
Claudia Winge<sup>8</sup>, Eric Perlman<sup>18</sup>

<sup>1</sup> Universidade Federal de Santa Maria, Departamento de Física/CCNE, 97105-900, Santa Maria, RS, Brazil.

<sup>2</sup> Kavli Institute for Astronomy and Astrophysics, Peking University, Beijing, China.

<sup>3</sup> Department of Astronomy, School of Physics, Peking University, Beijing, China.

<sup>4</sup> Gemini Observatory, Northern Operations Center, 670 N. Aohoku Place, Hilo, HI 96720, USA.

<sup>5</sup> Laboratório Nacional de Astrofísica/MCT, Rua dos Estados Unidos 154, Itajubá, MG, Brazil.

<sup>6</sup> NAT – Universidade Cruzeiro do Sul, Rua Galvão Bueno, 868, São Paulo, SP, Brazil.

<sup>7</sup> Universidade Federal do Rio Grande do Sul, Instituto de Física, CP 15051, Porto Alegre 91501-970, RS, Brazil.

<sup>8</sup> Gemini Observatory, Southern Operations Center, Casilla 603, La Serena, Chile;

<sup>9</sup> Astrophysics Department, Center for Astrobiology (CSIC-INTA), Torrejon de Ardoz, 28850 Madrid, Spain.

<sup>10</sup> Instituto de Física de Cantabria, CSIC-UC, 39005 Santander, Spain.

<sup>11</sup> University of the Pacific, Department of Physics, 3601 Pacific Avenue, Stockton, CA 95211, USA

<sup>12</sup> Instituto de Astrofísica de Canarias, Calle Vía Láctea, s/n, E-38205, La Laguna, Tenerife, Spain.

<sup>13</sup> Departamento de Astrofísica, Universidad de La Laguna, E-38205, La Laguna, Tenerife, Spain.

<sup>14</sup> Departamento de Astronomía, Universidad de Chile, Casilla 36-D, Santiago, Chile.

<sup>15</sup> Department of Physics and Astronomy, Macquarie University, NSW 2109, Australia.

<sup>16</sup> Astrophysics Research Institute, Liverpool John Moores University, IC2, Liverpool Science Park 146 Brownlow Hill, Liverpool L3 5RF, United Kingdom.

<sup>17</sup> Department of Physics & Astronomy, University of Victoria, PO Box 1700, STN CSC Victoria, BC, V8W 2Y2, CANADA

<sup>18</sup> Department of Physics and Space Sciences, Florida Institute of Technology, 150 West University Boulevard, Melbourne, FL 32901, USA

13 June 2021

## ABSTRACT

We examine the stellar velocity dispersions ( $\sigma$ ) of a sample of 48 galaxies, 35 of which are spirals, from the Palomar nearby galaxy survey. It is known that for ultra-luminous infrared galaxies (ULIRGs) and merger remnants the  $\sigma$  derived from the near-infrared CO band-heads is smaller than that measured from optical lines, while no discrepancy between these measurements is found for early-type galaxies. No such studies are available for spiral galaxies – the subject of this paper. We used cross-dispersed spectroscopic data obtained with the Gemini Near-Infrared Spectrograph (GNIRS), with spectral coverage from 0.85 to 2.5  $\mu\text{m}$ , to obtain  $\sigma$  measurements from the 2.29  $\mu\text{m}$  CO band-heads ( $\sigma_{\text{CO}}$ ), and the 0.85  $\mu\text{m}$  calcium triplet ( $\sigma_{\text{CaT}}$ ). For the spiral galaxies in the sample, we found that  $\sigma_{\text{CO}}$  is smaller than  $\sigma_{\text{CaT}}$ , with a mean fractional difference of 14.3%. The best fit to the data is given by  $\sigma_{\text{opt}} = (46.0 \pm 18.1) + (0.85 \pm 0.12)\sigma_{\text{CO}}$ . This “ $\sigma$  discrepancy” may be related to the presence of warm dust, as suggested by a slight correlation between the discrepancy and the infrared luminosity. This is consistent with studies that have found no  $\sigma$ -discrepancy in dust-poor early-type galaxies, and a much larger discrepancy in dusty merger remnants and ULIRGs. That  $\sigma_{\text{CO}}$  is lower than  $\sigma_{\text{opt}}$  may also indicate the presence of a dynamically cold stellar population component. This would agree with the spatial correspondence between low  $\sigma_{\text{CO}}$  and young/intermediate-age stellar populations that has been observed in spatially-resolved spectroscopy of a handful of galaxies.

**Key words:** galaxies: active – galaxies: stellar populations – infrared: galaxies – galaxies: kinematics

## 1 INTRODUCTION

The empirical relationship between the stellar velocity dispersion ( $\sigma$ ) of the spheroidal component of galaxies and the mass of the super-massive black hole ( $M_\bullet$ ) at their center (e.g. Ferrarese & Merrit 2000; Gebhardt et al. 2000) has been extensively used to estimate  $M_\bullet$  in active and inactive galaxies. More direct determinations of  $M_\bullet$ , through stellar kinematics within the black hole’s sphere of influence, or broad emission line measurements, are only feasible for a limited number of objects, making the  $M_\bullet - \sigma$  relation a very useful alternative. Cosmological simulations suggest that the central super-massive black hole (SMBH) evolves together with the host galaxy and plays a fundamental role in its evolution (Di Matteo, Springel & Hernquist 2005; Springel, Di Matteo & Hernquist 2005; Bower et al. 2006; Nemmen et al. 2007), and this co-evolution may be the mechanism that leads to the  $M_\bullet - \sigma$  relation. The intrinsic scatter in the relation (i.e., the range of  $M_\bullet$  found for a given  $\sigma$ ) therefore contains information about the processes of galaxy and black hole evolution (e.g. Gültekin et al. 2009). Besides the  $M_\bullet - \sigma$  relation, stellar velocity dispersion measurements are also relevant for many other astrophysical applications, including the galaxy fundamental plane (e.g. Djorgovski & Davis 1987; Dressler et al. 1987; Falcón-Barroso, Peletier & Balcells 2002; Gebhardt et al. 2003; Bernardi et al. 2003; Valluri, Merrit & Emsellem 2004), the metallicity- $\sigma$  relation (e.g. Terlevich et al. 1981; Dressler 1984a; Bender, Burstein & Faber 1993), the  $V/\sigma$  ratio that is an important criterium to determine the dynamical state of early type galaxies (e.g. Cox et al. 2006; Cappellari et al. 2007; Naab et al. 2013), etc. For all of these reasons, understanding the factors affecting  $\sigma$  measurements is an important issue.

Measurements of  $\sigma$  in galaxies have traditionally been done at wavelengths  $<1 \mu\text{m}$ , often using the “Mg b” line at  $0.52 \mu\text{m}$ , or the  $0.85 \mu\text{m}$  calcium triplet absorption (e.g. Ho et al. 2009). Measurements based on stellar absorption lines in the infrared (IR), on the other hand, can also probe regions that are obscured by dust at optical wavelengths, or different stellar populations from those revealed in the optical. For these reasons, several recent studies have compared  $\sigma$  values obtained from the fitting of stellar absorptions in the optical and in the near-IR spectral regions, generally using the CO absorption band heads in the H and K bands (Silge & Gebhardt 2003; Rothberg & Fischer 2010; Vanderbeke et al. 2011; Rothberg et al. 2013; Kang et al. 2013).

Silge & Gebhardt (2003) presented stellar velocity dispersions measured from the  $2.29\mu\text{m}$  CO band head in a sample composed of 18 lenticular (S0) and 7 elliptical galaxies. The resulting sigma values were compared with literature values derived primarily from fitting the Ca II lines near 4000 Å, the Mgb lines near 5175 Å, and the  $8500\text{Å}$  Ca II triplet (hereafter CaT). The  $\sigma_{\text{CO}}$  values were found to be up to 30% smaller than  $\sigma_{\text{opt}}$ , with a median difference of 11%. However, this difference was observed only in the lenticular galaxies; in the elliptical galaxies, the optical and IR measurements were consistent. The authors speculate that the difference may be related to the presence and distribution of dust in the S0 objects: if the dust is mainly located in the stellar disk, optical  $\sigma$  measurements will be biased towards the less-obscured, dynamically hotter bulge component.  $<1 \mu\text{m}$ .

Vanderbeke et al. (2011) measured  $\sigma_{\text{CO}}$  in a sample of 19 For-

nax cluster members, composed of roughly equal numbers of elliptical and lenticular galaxies. These measurements were compared with  $\sigma_{\text{opt}}$  from Kuntschner (2000) and found to be consistent, with  $\sigma_{\text{frac}} = \frac{\sigma_{\text{CO}} - \sigma_{\text{opt}}}{\sigma_{\text{opt}}} = 6.4\%$ . The lack of a discernible difference between  $\sigma_{\text{CO}}$  and  $\sigma_{\text{opt}}$  in the lenticular galaxies does not agree with the findings of Silge & Gebhardt (2003). It is, however, consistent with a previous study of velocity dispersions in the Fornax cluster by Silva et al. (2008).

Optical and IR velocity dispersions were also compared by Kang et al. (2013). This work used the CO absorption bands around  $1.6 \mu\text{m}$ , rather than those near  $2.3 \mu\text{m}$ , to derive  $\sigma_{\text{CO}}$  for 31 galaxies: 19 elliptical, 9 lenticular, and 3 spiral. No significant difference was found between  $\sigma_{\text{CO}}$  and  $\sigma_{\text{opt}}$  (based mainly on the CaT). This suggests that both sets of lines probe roughly the same stars, and provides no evidence for a dynamically cold, obscured population.

Rothberg & Fischer (2010) also compared  $\sigma_{\text{CO}}$  and  $\sigma_{\text{CaT}}$  for a set of galaxies. This time, however, they studied 14 galaxy mergers, accompanied by a control sample of 23 elliptical galaxies. The measurements for the control sample were taken mostly from the literature, and  $\sigma_{\text{CO}}$  and  $\sigma_{\text{CaT}}$  were found to be similar, in agreement with the studies above. On the other hand, large differences are found for the mergers. In particular, for luminous infrared galaxies (LIRGS, 6 objects in their sample) the  $\sigma$  derived in the optical is up to twice the value obtained for the near-IR. For the remaining 8 non-LIRG mergers,  $\sigma_{\text{CaT}}$  is slightly larger than  $\sigma_{\text{CO}}$ . Even larger discrepancies have been found for single nucleus Ultra-Luminous Infrared Galaxies (ULIRGs), for which  $\sigma_{\text{CaT}}$  can be three times larger than  $\sigma_{\text{CO}}$  (Rothberg et al. 2013). The discrepancies arise because  $\sigma_{\text{CO}}$ , although conveniently insensitive to dust absorption, probes a luminous, young stellar disk, whereas  $\sigma_{\text{CaT}}$  gives information about an older stellar population that is more representative of the galaxy’s overall dynamical mass. CO-based  $\sigma$  measurements imply that ULIRGs cannot be the progenitors of giant elliptical galaxies, whereas CaT-based values are consistent with a range of final galaxy masses.

The above studies have compared optical and CO-based  $\sigma$  measurements for early-type (E and S0) galaxies, and for galaxy mergers and ULIRGs. Little information is available, though, for late-type (spiral) objects, so the range of morphological types in which the large differences between  $\sigma_{\text{CO}}$  and  $\sigma_{\text{CaT}}$  occur is not yet known. We aim to rectify this situation by measuring  $\sigma_{\text{CO}}$  and  $\sigma_{\text{CaT}}$  in a sample of 48 nearby galaxies: 35 spirals, 7 lenticulars, and 6 ellipticals. We do this using slit spectroscopy covering simultaneously the CaT and  $2.29 \mu\text{m}$  CO spectral regions. In Section 2, we describe the sample and the observational data, and in Section 3 we discuss the methods used to measure the stellar dispersion in the optical and in the near-IR. The results are presented in Section 4, while their implications are discussed in Section 5. The conclusions of the present paper are given in Section 6.

## 2 OBSERVATIONS AND DATA REDUCTION

The sample of galaxies used in this work comprises 48 objects selected from the Palomar spectroscopic survey of nearby galaxies (Ho, Filippenko & Sargent 1995, 1997), covering a wide range of luminosity and nuclear activity type. Some properties of the sample are shown in Table 1, while full details of the overall program, sample, observations and data reduction are given in Mason et al. (submitted).

Briefly, the spectroscopic data were obtained in queue mode<sup>1</sup> with the Gemini Near-Infrared Spectrograph (GNIRS) on the Gem-

<sup>0</sup> We use  $\sigma_{\text{CO}}$  to denote velocity dispersions derived from the  $2.29 \mu\text{m}$  CO bands;  $\sigma_{\text{CaT}}$  for those based on the CaT lines; and  $\sigma_{\text{opt}}$  as a general term to include all measurements based on lines at  $\lambda$

ini North telescope. The cross-dispersed mode was used with the 32 l/mm grating, providing simultaneous spectral coverage from approximately 0.85 to 2.5  $\mu\text{m}$ . We used the  $0'.3 \times 7''$  slit, generally oriented along the mean parallactic angle at the time of the observations to minimize differential refraction effects. The data were obtained between October 2011 and May 2013. Due to work done to address an issue with the 32 l/mm grating mount in 2012, the spectral resolution of the spectra obtained with the  $0'.3$  slit after November 2012 differs from that achieved previously. The spectral resolution before November 2012 is 11.6  $\text{\AA}$  and 4.4  $\text{\AA}$  for the K-band CO band heads and the CaT regions, respectively, obtained from the full width at half maximum (FWHM) of the arc lamp calibration spectra. These values correspond to a resolution in velocity dispersion of  $\sim 65 \text{ km s}^{-1}$  for both regions. After November 2012, the resulting spectral resolutions are 18.2  $\text{\AA}$  and 7.4  $\text{\AA}$  corresponding to  $\sim 100 \text{ km s}^{-1}$  and  $\sim 110 \text{ km s}^{-1}$ .

The data were reduced using standard procedures<sup>2</sup>. To summarize, the raw frames are first cleaned of any electronic striping and cosmic ray-like features arising from  $\alpha$  particles in the camera lens coatings. The files are divided by a flat field and sky-subtracted using blank sky exposures made between the on-source observations, then rectified using pinhole images. Wavelength calibration is achieved using argon arc spectra, then a spectrum of each order is extracted, divided by a standard star to cancel telluric absorption lines, and roughly flux-calibrated using the telluric standard star spectrum. The individual orders are then combined to produce the final spectrum. The extraction aperture used for this work was  $1''.8$  along the  $0'.3$  slit, corresponding to a few tens to a few hundreds of parsecs at the distances of these galaxies.

### 3 METHODS

In order to obtain the line-of-sight velocity distribution (LOSVD) we have used the penalized Pixel-Fitting (pPXF) method of Cappellari & Emsellem (2004) to fit the CO absorption band heads around 2.3  $\mu\text{m}$  in the K-band and the Ca II  $\lambda 8500, 8544, 8665$  (the CaT) stellar absorptions in the Z band. The best fit of the galaxy spectrum is obtained by convolving template stellar spectra with the corresponding LOSVD, assumed to be well represented by Gauss-Hermite series. The pPXF method outputs the radial velocity, velocity dispersion ( $\sigma$ ) and higher order Gauss-Hermite moments ( $h_3$  and  $h_4$ ), as well as the uncertainties for each parameter. The  $h_3$  and  $h_4$  moments measure deviations of the line of sight velocity distribution from a Gaussian curve: the parameter  $h_3$  measures asymmetric deviations (e.g. wings) and the  $h_4$  quantifies the peakiness of the profile, with  $h_4 > 0$  and  $h_4 < 0$  indicating narrower and broader profiles than Gaussian, respectively (van der Marel & Franx 1993; Riffel 2010).

The dominant source of error in the velocity dispersion is usually related to the choice of stellar template used to fit the galaxy spectrum (e.g. Barth, Ho & Sargent 2002b; Riffel et al. 2008; Winge, Riffel & Storchi-Bergmann 2009). This can be minimized by using a large stellar template library, instead of the spectrum of a single star. The pPXF allows the use of several stellar template spectra, and varies the weighting of each one to obtain the best match to the observed spectrum, minimizing

issues arising from template mismatches. The set of templates must include stars that closely match the fitted galaxy spectrum (e.g. Silge & Gebhardt 2003; Emsellem et al. 2004; Riffel et al. 2008). For the fitting of the CO absorptions, we used as template spectra those of the Gemini Near-IR Late-type stellar library (Winge, Riffel & Storchi-Bergmann 2009), which contains spectra of 60 stars with spectral types ranging from F7 III to M5 III, observed in the K band at a spectral resolution of  $\sim 3.2 \text{\AA}$  (FWHM).

As template spectra for the CaT region, we used selected spectra of stars from the CaT stellar library of Cenarro et al. (2001) with a spectral resolution of 1.5  $\text{\AA}$  (FWHM). This library contains spectra of 706 stars with all spectral types and is part of the Medium-resolution Isaac Newton Telescope library (MILES; Sánchez-Blázquez et al. 2006). In this work, we used only the spectra of stars with S/N ratio larger than 50 in the CaT region in order to avoid the selection of noisy spectra by the pPXF code. The final template library contains 190 spectra, including several spectral types. We also tested the NASA InfraRed Telescope Facility (IRTF) stellar spectral library (Cushing, Rayner, & Vacca 2005; Rayner, Cushing, & Vacca 2009) that presents spectra of late-type stars ranging from 0.8 to 5.5  $\mu\text{m}$  at a spectral resolving power of  $R = \lambda/\Delta\lambda \sim 2000$ , similar to the spectral resolution used in this work. The comparison of the kinematic parameters obtained with the IRTF spectral library are similar to the ones obtained with the two libraries mentioned above. However, the standard deviation of the residuals (defined as the difference between the galaxy spectrum and the best fit model) and the uncertainties are much larger using the IRTF library. This may be related to the S/N ratio of the IRTF spectra, and/or their lower spectral resolution compared to the MILES library. We therefore decided to use the Gemini and MILES libraries for this work.

Since the spectral resolution of the template stellar spectra for both spectral regions is better than the resolution of our observations, we degraded the stellar templates to the same resolution as the spectra of the galaxies before running the pPXF to measure the LOSVD. In order to properly fit the continuum emission we allowed pPXF to fit multiplicative Legendre polynomials of order 1 to account for any slope introduced by dust/AGN emission. Since the order of the polynomials included is small, they do not introduce any bias in the derived stellar kinematics.

Although pPXF outputs the errors of the measurements, we also performed 100 iteration of Monte Carlo simulations where random noise was introduced to the galaxy spectrum, keeping constant the signal-to-noise ratio and the standard deviation of the 100 measurements for each galaxy. The errors obtained from the simulations are similar to the uncertainties that pPXF outputs.

Figure A1 shows the fits of the galaxy spectra at the region of the CO band heads (2.25–2.41  $\mu\text{m}$ ) for all the galaxies of our sample. The fits reproduce the observed spectra very well for all objects, with the residuals being smaller than 3 times the standard deviation of the continuum emission next to the CO absorptions. Two objects (NGC 2273 and NGC 4388) present strong  $[\text{C IV}] 2.322 \mu\text{m}$  line emission superimposed on the second  $^{12}\text{CO}$  absorption band head, so this band was excluded from the fitted region.

The fits for the CaT spectral region (8480–8730  $\text{\AA}$ ) are shown in Figure A2. They also reproduce the observed spectra well, with the residuals again generally being smaller than 3 times the standard deviation of the continuum emission next to the CaT. However, for some objects the residuals are somewhat larger (e.g. NGC 5194, NGC 5371, NGC 7743, and NGC 7332 – see bottom panels of Fig. A2) due to the lower S/N ratio of those spectra in

<sup>1</sup> Programs GN-2011B-Q-111, GN-2012A-Q-23, GN-2012B-Q-80, GN-2012B-Q-112, GN-2013A-Q-16.

<sup>2</sup> Described at [www.gemini.edu/sciops/instruments/gnirs/data-format-and-reduction/reducing-xd-spectra](http://www.gemini.edu/sciops/instruments/gnirs/data-format-and-reduction/reducing-xd-spectra).

this region. This results in uncertainties of up to  $25 \text{ km s}^{-1}$  in the resulting velocity dispersions.

For the CO spectral region, we find that  $\sigma_{CO}$  is smaller than the spectral resolution of the spectra for 3 objects (NGC 205, NGC 404 and NGC 5194), while for the CaT region only the dwarf elliptical NGC 205 has  $\sigma$  smaller than the resolution. These values are marked by \* in Table 1 and should be considered highly uncertain. In particular, for the galaxies NGC 205 and NGC 404, Ho et al. (2009) measured values lower than our resolution, using higher-resolution data.

## 4 RESULTS

The major difference and main advantage of the present work, compared to previous studies, is that we measure both  $\sigma_{CO}$  and  $\sigma_{CaT}$  from the same spectra, observed in the same way, with the same aperture and using the same method, while previous studies used their own  $\sigma_{CO}$  measurements and compared them with optical  $\sigma$  values from the literature. Resulting measurements of the stellar velocity dispersion and Gauss-Hermite moments for our sample are shown in Table 1.

In Figure 1 we show  $\sigma_{CO}$  vs  $\sigma_{CaT}$ , excluding objects for which good fits could not be obtained for one of the spectral regions (marked by dashes in the Table 1). We find that  $\sigma_{CaT}$  tends to be higher than  $\sigma_{CO}$ , with an average difference of  $\sigma_{CO} - \sigma_{CaT} = -19.2 \pm 5.6 \text{ km s}^{-1}$  (for all morphological types). The error in this value was obtained using Monte Carlo simulations and the bootstrap technique (e.g. Beers, Flynn & Gebhardt 1990) as follows. First, 10000 Monte Carlo iterations were run to determine the effect to the uncertainties in  $\sigma$  to the mean sigma difference ( $\langle \sigma_{CO} - \sigma_{CaT} \rangle$ ). At each run, random values for  $\sigma_{CO}$  and  $\sigma_{CaT}$  constrained to be within their measured uncertainties were generated and then the  $\langle \sigma_{CO} - \sigma_{CaT} \rangle$  was calculated. The standard deviation of the 10000 simulations of  $\langle \sigma_{CO} - \sigma_{CaT} \rangle$  ( $\epsilon_{\sigma_u}$ ) represents the effects of the uncertainties in  $\sigma$  to the  $\langle \sigma_{CO} - \sigma_{CaT} \rangle$ . Then, to evaluate the completeness of the sample and its effect to the mean  $\sigma$  difference, we run a bootstrap with 10000 realizations in which for each iteration the  $\langle \sigma_{CO} - \sigma_{CaT} \rangle$  is calculated for a sample selected randomly among the galaxies of our sample. The standard deviation of the simulated  $\langle \sigma_{CO} - \sigma_{CaT} \rangle$  ( $\epsilon_{\sigma_s}$ ) represents the intrinsic scatter of our sample. Finally, the uncertainty  $\epsilon_{\langle \sigma_{CO} - \sigma_{CaT} \rangle}$  is obtained by the sum of  $\epsilon_{\sigma_u}$  and  $\epsilon_{\sigma_s}$  in quadrature, as  $\epsilon_{\langle \sigma_{CO} - \sigma_{CaT} \rangle} = \sqrt{(\epsilon_{\sigma_u}^2 + \epsilon_{\sigma_s}^2)} = \sqrt{(2.6 \text{ km s}^{-1})^2 + (4.6 \text{ km s}^{-1})^2} = 5.6 \text{ km s}^{-1}$ . This value is similar to the standard error. If we exclude also the 3 objects with  $\sigma$  values smaller than the instrumental broadening, we find  $\sigma_{CO} - \sigma_{CaT} = -17.7 \pm 5.7 \text{ km s}^{-1}$ .

We also performed a Kolmogorov-Smirnov test to determine if  $\sigma_{CaT}$  and  $\sigma_{CO}$  differ significantly. We found a statistic significance  $P = 0.2$  for our sample, where  $P$  ranges from 0 to 1 and small values mean that the two data sets are significantly different. The value of  $P$  obtained for our sample indicates that there is a reasonable probability (80 %) that  $\sigma_{CaT}$  and  $\sigma_{CO}$  present discrepant values.

The comparisons of higher order Gauss-Hermite moments  $h_3$  and  $h_4$  obtained from the fitting of the CaT with those of the CO band heads show an average differences of  $h_{3CO} - h_{3CaT} = -0.01 \pm 0.03$  and  $h_4$  is  $h_{4CO} - h_{4CaT} = 0.07 \pm 0.03$ . For both the  $h_3$  and  $h_4$  parameters there is no correlation between the values found from the fitting of the CaT and the ones from the CO band heads. The values found for  $h_3$  and  $h_4$  are small for most of the objects in our sample, indicating that the LOSVD of the stars for the nucleus of

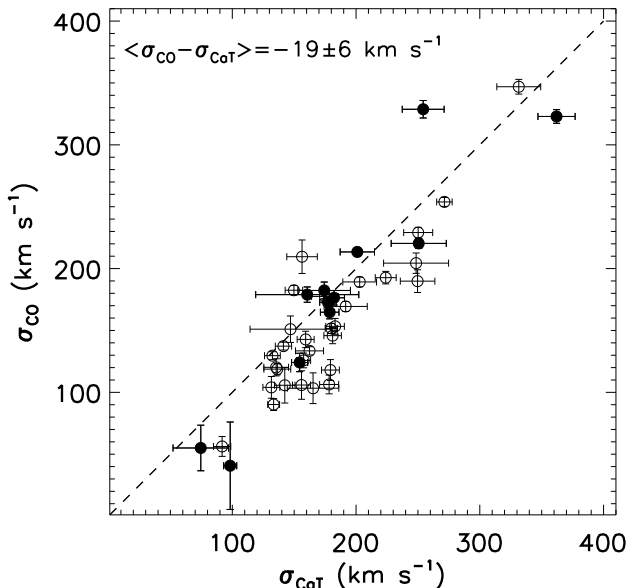


**Figure 1.** Comparison between the stellar velocity dispersion obtained from the fitting of the CO band heads (y-axis) and from the fitting of the CaT (x-axis). The dashed line shows a one-to-one relation. Filled circles are for the elliptical and lenticular galaxies of our sample and open circles represent the spiral galaxies.

these galaxies is reasonably well reproduced by a Gaussian velocity distribution.

## 5 ANALYSIS OF THE RESULTS

To understand the observed difference between  $\sigma_{CO}$  and  $\sigma_{CaT}$  in the galaxies, we performed several tests to identify possible systematic effects in the data or introduced by the fitting procedure.

As discussed in Sec. 3, we were very careful in the estimation of the instrumental broadening, taking into account the facts that (i) our observations present distinct spectral resolutions depending on the date of the observations, and (ii) the spectral resolution for observations performed after November 2012 differs between the CaT and CO regions (§2). The uncertainty (rms) in the FWHM of the arc lamp lines is smaller than  $10 \text{ km s}^{-1}$  for both spectral regions and in order to “correct” the offset from the one-to-one relation observed in  $\sigma$  in Fig. 1 the FWHM in the CaT region would have to be underestimated by more than  $30 \text{ km s}^{-1}$ . Thus, uncertainties in the instrumental broadening cannot account for the observed differences in CaT- and CO-based  $\sigma$  values in our sample.

As noted in §3, template mismatch could also introduce systematic uncertainties in the  $\sigma$  measurements (e.g. Silge & Gebhardt 2003; Riffel et al. 2008). Usually fewer than 10 template spectra are needed by pPXF to successfully reproduce the CO absorption band heads and the CaT. Although the libraries used here are large and contain spectra of stars with several spectral types, the fits to both spectral regions are dominated by giant and super-giant stars, with a slightly larger contribution from super-giants in the K band. These are the spectral types that are expected to dominate the emission in the near-IR, suggesting that pPXF is selecting the appropriate stars with which to fit the spectra. For most galaxies M-stars are the dominant contributor to the fits in the K-band, while K-stars dominate in the region of the CaT. The difference between the intrinsic widths of the absorption lines in these stars is  $\sim 10 \text{ km s}^{-1}$ , which

**Table 1.** Properties of the galaxies from our sample. Col. 1: Name of the object. Col. 2: Morphological type from Ho, Filippenko & Sargent (1997). Col. 3: Nuclear Activity from Ho, Filippenko & Sargent (1997) - S: Seyfert nucleus, L: LINER, T: Transition object and H: H II nucleus. “:” means that the classification is uncertain. Cols 4 – 9: Stellar kinematic parameters. Col 10: The instrumental configuration used for the observations. Configuration “a” corresponds to observations done before November 2012 and has an instrumental  $\sigma$  of 65 km s<sup>-1</sup> for both spectral regions. Configuration “b” corresponds to observations done after November 2012 and has an instrumental  $\sigma$  of 100 and 110 km s<sup>-1</sup> for the CO and CaT regions. The uncertainties included for the kinematic parameters are those that pPXF outputs. The dashes in the table are due to the fact that for a few objects we were not able to get a good fit of the spectrum in one of the spectral regions due to a low signal-to-noise ratio or non-detection of the absorption lines.

Object	Hubble Type	N. A.	$\sigma_{CO}$ (km/s)	$\sigma_{CaT}$ (km/s)	$h_{3CO}$	$h_{3CaT}$	$h_{4CO}$	$h_{4CaT}$	Conf.
NGC 205	dE5 pec	–	40.7± 35.3*	98.3±5.3*	0.00± 0.15	0.00± 0.05	0.01± 0.12	-0.13± 0.03	b
NGC 266	SB(rs)ab	L1.9	204.4± 8.2	248.5± 26.3	0.00± 0.02	0.04± 0.07	0.07± 0.03	0.01± 0.08	a
NGC 315	E+:	L1.9	322.9± 5.5	362.0± 15.0	0.02± 0.02	0.03± 0.04	-0.08± 0.02	-0.20± 0.03	a
NGC 404	SA(s)0-:	L2	55.0± 18.4*	74.5± 22.5	-0.02± 0.13	-0.02± 0.19	0.03± 0.20	-0.03± 0.16	a
NGC 410	E+:	T2	276.4± 20.0	–	-0.05± 0.05	–	-0.03± 0.06	–	a
NGC 474	(R’)SA(s)0	L2:	164.8± 5.4	178.7± 7.5	0.03± 0.02	0.06± 0.04	0.06± 0.02	-0.05± 0.04	a
NGC 660	SB(s)a pec	T2/H	164.7±17.3	–	-0.05±0.06	–	0.12± 0.07	–	b
NGC 1052	E4	L1.9	220.3± 4.1	250.6± 22.3	-0.01± 0.01	-0.07± 0.05	0.03± 0.01	0.04± 0.06	a
NGC 1167	SA0-	S2	179.0± 6.2	160.6± 41.7	0.01± 0.02	0.03± 0.06	0.00± 0.03	0.00± 0.21	a
NGC 1358	SAB(r)0/a	S2	182.3± 6.8	174.3± 21.2	-0.03± 0.03	0.08± 0.10	-0.03± 0.03	-0.09± 0.09	a
NGC 1961	SAB(rs)c	L2	189.9± 9.2	249.7± 13.9	0.01± 0.02	0.03± 0.05	0.11± 0.03	-0.07± 0.04	b
NGC 2273**	SB(r)a:	S2	105.7± 14.4	142.4± 8.3	-0.11± 0.06	0.05± 0.04	0.03± 0.09	0.02± 0.05	b
NGC 2639	(R)SA(r)a?	S1.9	160.4± 5.2	–	0.02± 0.02	–	-0.04± 0.03	–	a
NGC 2655	SAB(s)0/a	S2	145.8± 6.5	181.1± 7.1	0.02± 0.02	0.03± 0.03	0.08± 0.03	0.01± 0.03	b
NGC 2768	E6:	L2	172.8± 3.8	177.3± 6.7	0.01± 0.01	-0.05± 0.03	0.02± 0.02	0.04± 0.03	a
NGC 2832	E+2:	L2:	328.7± 7.1	254.2± 16.9	0.06± 0.02	0.02± 0.05	-0.01± 0.02	-0.03± 0.05	b
NGC 3031	SA(s)ab	S1.5	182.5± 3.8	149.8± 7.1	0.00± 0.01	0.04± 0.03	0.08± 0.01	0.03± 0.04	a
NGC 3079	SB(s)c spin	S2	143.6± 4.7	–	-0.01±0.02	–	0.05±0.02	–	a
NGC 3147	SA(rs)bc	S2	229.1± 4.2	250.2± 11.7	0.00± 0.01	0.02± 0.03	0.06± 0.01	0.03± 0.03	b
NGC 3169	SA(s)a pec	L2	169.4± 4.0	191.6± 17.5	0.01± 0.02	0.13± 0.04	0.01± 0.02	0.04± 0.06	a
NGC 3190	SA(s)a pec spin	L2	189.2± 3.9	202.9± 13.6	0.02± 0.01	0.00± 0.06	0.06± 0.01	-0.07± 0.05	a
NGC 3607	SA(s)0:	L2	213.5± 3.6	201.0± 13.9	0.01± 0.01	0.00± 0.07	0.06± 0.01	-0.09± 0.06	a
NGC 3718	SB(s)a pec	L1.9	192.7± 5.1	224.0± 8.4	-0.03± 0.01	-0.04± 0.03	0.08± 0.02	-0.01± 0.03	b
NGC 3998	SA(s)ab	L1.9	346.9± 5.9	331.5± 17.7	0.02± 0.01	-0.03± 0.04	-0.02± 0.02	0.03± 0.04	b
NGC 4203	SAB0-:	L1.9	176.4± 5.9	182.2± 8.4	0.00± 0.02	-0.02± 0.04	0.03± 0.02	-0.05± 0.04	b
NGC 4235	SA(s)a spin	S1.2	209.6± 13.5	156.4± 12.3	-0.10± 0.03	0.01± 0.05	0.12±0.03	0.06± 0.05	b
NGC 4258	SAB(s)b	S1.9	129.6± 3.2	132.4± 6.4	-0.02± 0.01	-0.02± 0.04	0.02± 0.02	-0.05± 0.04	a
NGC 4346	SA0 spin	L2:	124.1± 7.4	154.4± 6.5	0.00± 0.02	0.06± 0.02	0.07± 0.04	0.00± 0.03	b
NGC 4388**	SA(s)b: spin	S1.9	103.3± 12.4	165.3± 20.8	-0.01± 0.05	0.01± 0.09	0.01± 0.08	0.01± 0.09	b
NGC 4450	SA(s)ab	L1.9	118.8± 4.6	136.4± 10.9	0.00± 0.02	-0.07± 0.05	0.08± 0.03	-0.05± 0.07	a
NGC 4548	SB(rs)b	L2	104.0± 8.8	131.6± 6.8	0.00± 0.03	0.00± 0.04	0.04± 0.06	0.02± 0.04	b
NGC 4565	SA(s)b? spin	S1.9	151.6± 4.0	180.0± 5.0	0.03± 0.01	-0.01± 0.02	0.02± 0.02	-0.04± 0.02	b
NGC 4569	SAB(rs)ab	T2	106.4± 7.6	178.2±7.8	-0.05± 0.03	0.08±0.02	0.03± 0.05	0.05±0.03	b
NGC 4579	SAB(rs)b	S1.9/L1.9	177.5± 5.3	174.9± 10.8	0.05± 0.02	0.03± 0.04	0.06± 0.02	0.01± 0.05	a
NGC 4594	SA(s)a spin	L2	253.9± 3.6	271.4± 6.3	0.00± 0.01	0.03± 0.02	0.06± 0.01	-0.01± 0.02	b
NGC 4725	SAB(r)ab pec	S2:	133.5± 3.3	162.4± 11.3	-0.05± 0.02	0.27± 0.08	-0.02± 0.02	-0.27± 0.07	a
NGC 4736	(R)SA(r)ab	L2	120.2± 6.9	135.4± 10.0	0.13± 0.04	0.01± 0.05	-0.05± 0.04	0.01± 0.06	b
NGC 4750	(R)SA(rs)ab	L1.9	105.9± 11.5	155.9± 7.3	-0.01± 0.03	-0.05± 0.04	0.08± 0.07	-0.08± 0.04	b
NGC 5005	SAB(rs)bc	L1.9	153.3± 6.4	183.1± 7.5	-0.01± 0.02	-0.01± 0.02	0.08± 0.03	0.06± 0.03	b
NGC 5033	SA(s)c	S1.5	151.0± 10.7	147.0± 32.7	-0.12± 0.04	0.04± 0.16	0.15± 0.05	-0.01± 0.22	a
NGC 5194	SA(s)bc pec	S2	56.3± 8.0*	91.8± 7.0	-0.02± 0.0	-0.04± 0.05	0.03± 0.09	-0.01± 0.05	a
NGC 5371	SAB(rs)bc	L2	142.8± 6.6	159.3± 6.8	-0.01± 0.02	0.01± 0.03	0.04± 0.03	-0.03± 0.04	b
NGC 5850	SB(r)b	L2	118.0± 8.5	179.3± 7.2	0.05± 0.03	0.02± 0.03	0.07± 0.05	-0.05± 0.03	b
NGC 6500	SAab:	L2	177.5± 5.6	–	0.00± 0.02	–	0.04± 0.02	–	a
NGC 7217	(R)SA(r)ab	L2	125.8± 5.9	157.6± 5.6	-0.01± 0.02	0.04± 0.02	0.03± 0.03	0.00± 0.03	b
NGC 7331	SA(s)b	T2	137.3± 3.2	141.3± 6.6	0.03± 0.01	-0.03± 0.04	0.01± 0.02	-0.05± 0.04	a
NGC 7743	(R)SB(s)0+	S2	90.2± 4.8	133.4± 4.8	0.04± 0.02	-0.13± 0.04	0.05± 0.04	-0.20± 0.03	a

\* The measured  $\sigma$  is smaller than the instrumental  $\sigma$ .

\*\* The second CO band was excluded from the fitting due to contamination by the [Caviii] 2.322 $\mu$ m emission.

is negligible compared to the overall difference between  $\sigma_{CaT}$  and  $\sigma_{CO}$  in the sample. In Appendix B we show the stellar templates used to fit the spectrum of each galaxy. Additionally, there is no difference in the  $\chi^2$  values of the fits between early and late-type galaxies, suggesting that there is no bias in the choice of template for each type of galaxy.

As several galaxies of our sample have a Seyfert nucleus, hot dust emission may play an important role in the K-band continuum. The CO band-heads can be “diluted” by this emission, which might introduce an uncertainty in the measurements of  $\sigma_{CO}$  (e.g. Ivanov et al. 2000; Riffel, Rodríguez-Ardila & Pastoriza 2006; Kotilainen et al. 2012). To test whether the pPXF accounts

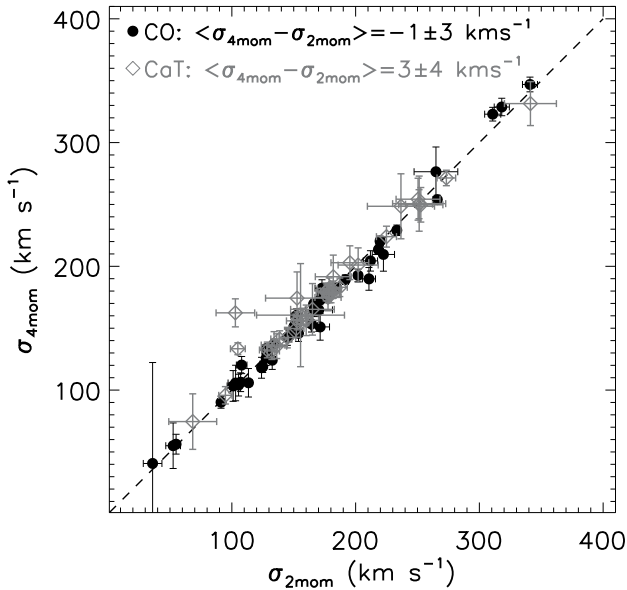


**Figure 2.** Comparison of  $\sigma$  values obtained from the fit of 2 and 4 moments in the LOSVD.

correctly for variations of the continuum shape, we have simulated contributions of Planck functions with temperatures ranging from 700 to 2000 K to the continuum emission at the K-band. No significant difference in  $\sigma_{\text{CO}}$  was found when including dust emission ranging from 1% to 70% of the total K-band emission. Furthermore, for the objects in which we could measure the  $\sigma$  from the H-band CO lines (where the contribution from AGN-heated dust is smaller; Origlia, Moorwood & Oliva 1993), it agrees to within 10% with that measured from the K-band and no systematic difference is found between H and K band measurements. Thus, we conclude that the hot dust emission plays a negligible role in the  $\sigma$  measurements.

In galaxies with low values of  $\sigma$ , the fitting of higher order Gauss-Hermite moments can introduce uncertainties in the  $\sigma$  measurements (see the *bias* parameter of the pPXF program; Cappellari & Emsellem 2004). To test this, we fitted the spectra of the galaxies assuming that the LOSVD is well described by a Gaussian, by fitting only the first 2 moments. In Fig. 2 we present the comparison of  $\sigma$  values obtained from the fitting of 4 moments with those obtained from the fitting of 2 moments. This figure shows that the resulting  $\sigma$  for both the CO and CaT spectral regions are very similar to those obtained when allowing the pPXF to include the  $h_3$  and  $h_4$  parameters, suggesting that the inclusion of these parameters does not affect significantly the  $\sigma$  measurements for our sample.

Finally, we compare our  $\sigma_{\text{CaT}}$  measurements with the optical  $\sigma$  values of Ho et al. (2009) for the same galaxies. Ho et al. (2009) used two spectral ranges to measure  $\sigma$ : a blue region, from 4200 to 5000 Å that includes several Fe lines, and a red region, covering the range 6450–6550 Å where Ca+Fe lines are present. They found that both values are in good agreement. In Fig. 3 we show our  $\sigma_{\text{CaT}}$  vs. the  $\sigma$  values presented in Ho et al. (2009). This comparison shows that 50% of the objects have  $\sigma$  differences smaller than 10% and for about 90% of the objects the differences are smaller than 25%, indicating that our measurements are in agreement with those from Ho et al. (2009). Differences between the measurements may be due to the larger aperture ( $2'' \times 4''$ ) used by Ho et al. (2009), as well as differences in the S/N ratio of the spectra and the exact measurement procedures used.

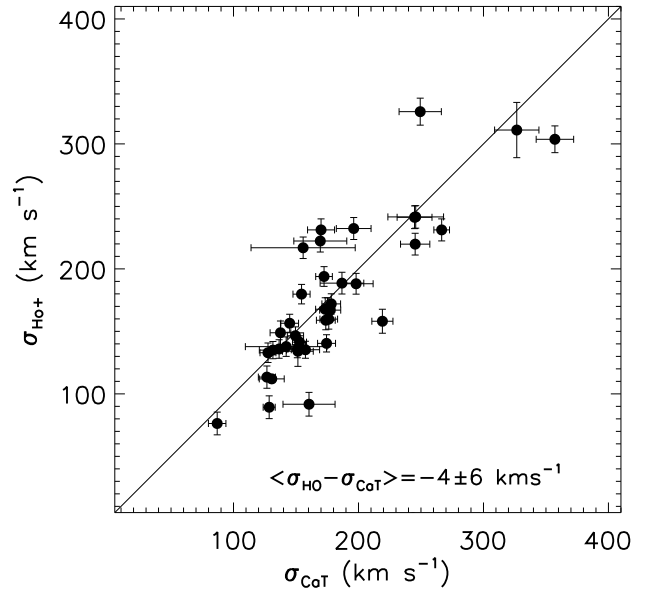


**Figure 3.** Comparison of  $\sigma_{\text{CaT}}$  with those found by Ho et al. (2009) using various optical lines.

We therefore conclude that our  $\sigma$  measurements are robust, and that the observed difference between  $\sigma_{\text{CaT}}$  and  $\sigma_{\text{CO}}$  is not due to measurement error.

## 6 DISCUSSION

We have found a systematic offset between  $\sigma_{\text{CO}}$  and  $\sigma_{\text{CaT}}$  in the galaxies in our sample, which are primarily spirals. In order to further investigate the  $\sigma$ -discrepancy in late-type galaxies and compare the results with the available studies of other galaxy types, we compiled values for the  $\sigma_{\text{CO}}$  and for optical measurements (most of them obtained from the CaT region) from the literature for distinct classes of objects. Table 2 presents the resulting  $\sigma_{\text{opt}}$  and  $\sigma_{\text{CO}}$  values for elliptical, lenticular and spiral galaxies and merger remnants. Since there is good agreement between the  $\sigma$  values obtained from CaT and those from the fitting of other optical lines (e.g. Barth, Ho & Sargent 2002a,b) and as not all the optical values from the literature were obtained from the CaT region, we will use the nomenclature “optical” velocity dispersion ( $\sigma_{\text{opt}}$ ) to refer to measurements of  $\sigma$  obtained from the CaT or other optical lines.

In order to investigate the relation between  $\sigma$  discrepancy and morphological classification, we plotted in Figure 4  $\sigma_{\text{opt}}$  vs.  $\sigma_{\text{CO}}$  for distinct classes of objects. The largest  $\sigma$  difference is observed for the merger remnants and ULIRGs, for which no correlation is found between  $\sigma_{\text{opt}}$  and  $\sigma_{\text{CO}}$  and the mean difference is  $\sigma_{\text{CO}} - \sigma_{\text{opt}} = -57.8 \pm 13.7 \text{ km s}^{-1}$ . Elliptical galaxies follow the one-to-one relation and no discrepancy between optical and near-IR measurements is found. The mean difference is  $\sigma_{\text{CO}} - \sigma_{\text{opt}} = -1.5 \pm 4.6 \text{ km s}^{-1}$ . For lenticulars, the mean difference is  $\sigma_{\text{CO}} - \sigma_{\text{opt}} = -10.8 \pm 6.4 \text{ km s}^{-1}$  and it can be seen from the figure that most points are distributed around the one-to-one relation. The best linear fit for lenticular galaxies is given by

$$\sigma_{\text{opt}} = (9.1 \pm 13.2) + (0.99 \pm 0.08)\sigma_{\text{CO}}, \quad (1)$$

shown as a dashed line in the bottom-left panel of Fig. 4.

For spiral galaxies we found a mean difference of  $\sigma_{\text{CO}} - \sigma_{\text{opt}} = -24.0 \pm 4.9 \text{ km s}^{-1}$ . Excluding NGC 5194, which presents a sigma

**Table 2.** Velocity dispersions compiled from the literature.

Object	$\sigma_{\text{CO}}(\text{km s}^{-1})$	$\sigma_{\text{opt}}(\text{km s}^{-1})$	Ref.	Object	$\sigma_{\text{CO}}(\text{km s}^{-1})$	$\sigma_{\text{opt}}(\text{km s}^{-1})$	Ref.
<b>ELLIPTICAL GALAXIES</b>				<b>LENTICULAR GALAXIES</b>			
NGC 221	71±8	75±4	[1]	NGC 1023	152±11	205±10	[1]
	70±2	75±3	[2]		217±5	205±10	[2]
	60±8	69±2	[4]	NGC 1161	274±19	297±17	[1]
NGC 315	321±59	310±16	[1]	NGC 1375	64±4	56±10	[3]
	324±59	351±16	[4]	NGC 1380	190±17	219±11	[3]
NGC 821	195±17	209±10	[1]	NGC 1380A	60±9	55±9	[3]
	208±5	209±10	[2]	NGC 1381	155±6	153±8	[3]
	188±17	197±20	[4]	NGC 1400	212±12	264±26	[1]
NGC 1052	211±20	196±4	[4]	NGC 2110	224±49	220±25	[1]
NGC 1316	212±20	243±9	[4]	NGC 2293	255±44	254±13	[1]
NGC 1336	119±8	96±5	[3]	NGC 2380	164±31	189±9	[1]
NGC 1339	182±9	158±8	[3]	NGC 2681	82±9	111±22	[1]
NGC 1344	158±20	166±7	[4]	NGC 2768	235±51	198±28	[1]
NGC 1351	153±7	157±8	[3]	NGC 2787	153±8	210±12	[1]
NGC 1373	80±5	75±4	[3]		186±3	189±9	[2]
NGC 1374	207±10	185±9	[3]	NGC 3115	272±12	230±11	[2]
	181±20	180±8	[4]	NGC 3245	206±7	205±10	[2]
NGC 1379	130±7	130±7	[3]	NGC 3384	151±3	143±7	[2]
	126±20	127±5	[4]	NGC 3998	205±16	297±15	[1]
NGC 1399	406±33	375±19	[3]	NGC 4150	113±18	132±10	[1]
	336±20	325±15	[4]	NGC 4342	224±5	225±11	[2]
NGC 1404	247±22	260±13	[3]	NGC 4564	175±7	162±8	[2]
	204±20	230±10	[4]	NGC 4596	139±3	136±6	[2]
NGC 1407	297±40	283±13	[4]	NGC 5195	95±6	175±30	[1]
	306±40	285±40	[1]	NGC 5866	186±14	139±7	[1]
NGC 1419	125±5	117±6	[3]	NGC 6548	225±47	307±23	[1]
	116±20	110±6	[4]	NGC 6703	146±42	186±9	[1]
NGC 1427	155±18	175±9	[3]	NGC 7332	148±13	130±10	[1]
	174±20	172±8	[4]	NGC 7457	63±2	67±3	[2]
NGC 2778	161±4	175±8	[2]	NGC 7743	66±12	83±20	[1]
NGC 2974	272±19	262±13	[1]	IC 1963	49±6	58±10	[3]
	262±19	255±12	[4]	ESO 358-G06	55±25	58±11	[3]
NGC 3377	144±20	145±7	[1]	ESO 358-G59	70±20	54±9	[3]
	147±4	145±7	[2]	<b>SPIRAL GALAXIES</b>			
	134±20	135±4	[4]	NGC 1068	129±3	151±7	[2]
NGC 3379	235±20	185±2	[4]	NGC 3031	157±3	143±7	[2]
NGC 3607	210±8	229±11	[2]	NGC 4258	111±2	115±10	[2]
NGC 3608	187±4	182±9	[2]	<b>MERGER REMNANTS/ULIRGS</b>			
NGC 4261	286±6	315±15	[2]	NGC 1614	133±3	219±3	[4]
NGC 4291	248±7	242±12	[2]	NGC 2418	245±7	282±3	[4]
NGC 4365	262±20	240±3	[4]	NGC 2623	152±4	174±3	[4]
NGC 4374	290±8	296±14	[2]	NGC 2914	179±6	178±2	[4]
NGC 4459	164±6	167±8	[2]	NGC 3256	111±20	239±4	[4]
NGC 4472	291±20	269±3	[4]	NGC 4194	98±25	103±2	[4]
NGC 4473	186±3	190±9	[2]	NGC 5018	243±7	222±2	[4]
NGC 4486	310±20	361±37	[4]	NGC 7252	119±19	160±3	[4]
	331±11	375±18	[2]	Arp 193	143±5	229±4	[4]
NGC 4649	327±11	385±19	[2]	IC 5298	150±28	187±4	[4]
NGC 4697	172±4	177±8	[2]	AM 0612-373	240±9	286±9	[4]
NGC 4742	104±3	90±5	[2]	AM 1419-263	262±6	258±3	[4]
NGC 5128	190±13	145±6	[4]	AM 2038-382	207±4	256±5	[4]
NGC 5812	230±6	248±2	[4]	AM 2055-425	137±15	207±7	[4]
NGC 5845	237±4	234±11	[2]	IRAS 02021-2103	143±21	209±8	[5]
NGC 6251	290±8	290±14	[2]	IRAS 05189-2524	131±16	265±7	[5]
NGC 7052	327±13	266±13	[2]	IRAS 12540-5708	117±10	346±9	[5]
NGC 7619	246±47	296±15	[1]	IRAS 17208-0014	223±15	261±5	[5]
	246±47	296±11	[4]	IRAS 23365-3604	143±15	221±6	[5]
NGC 7743	66±12	83±20	[1]				
NGC 7626	313±20	265±10	[4]				
IC 2006	125±10	136±7	[3]				

[1] - Silge & Gebhardt (2003); [2] - Kang et al. (2013); [3] - Vanderbeke et al. (2011)  
 [4] - Rothberg & Fischer (2010), [5] - Rothberg et al. (2013)

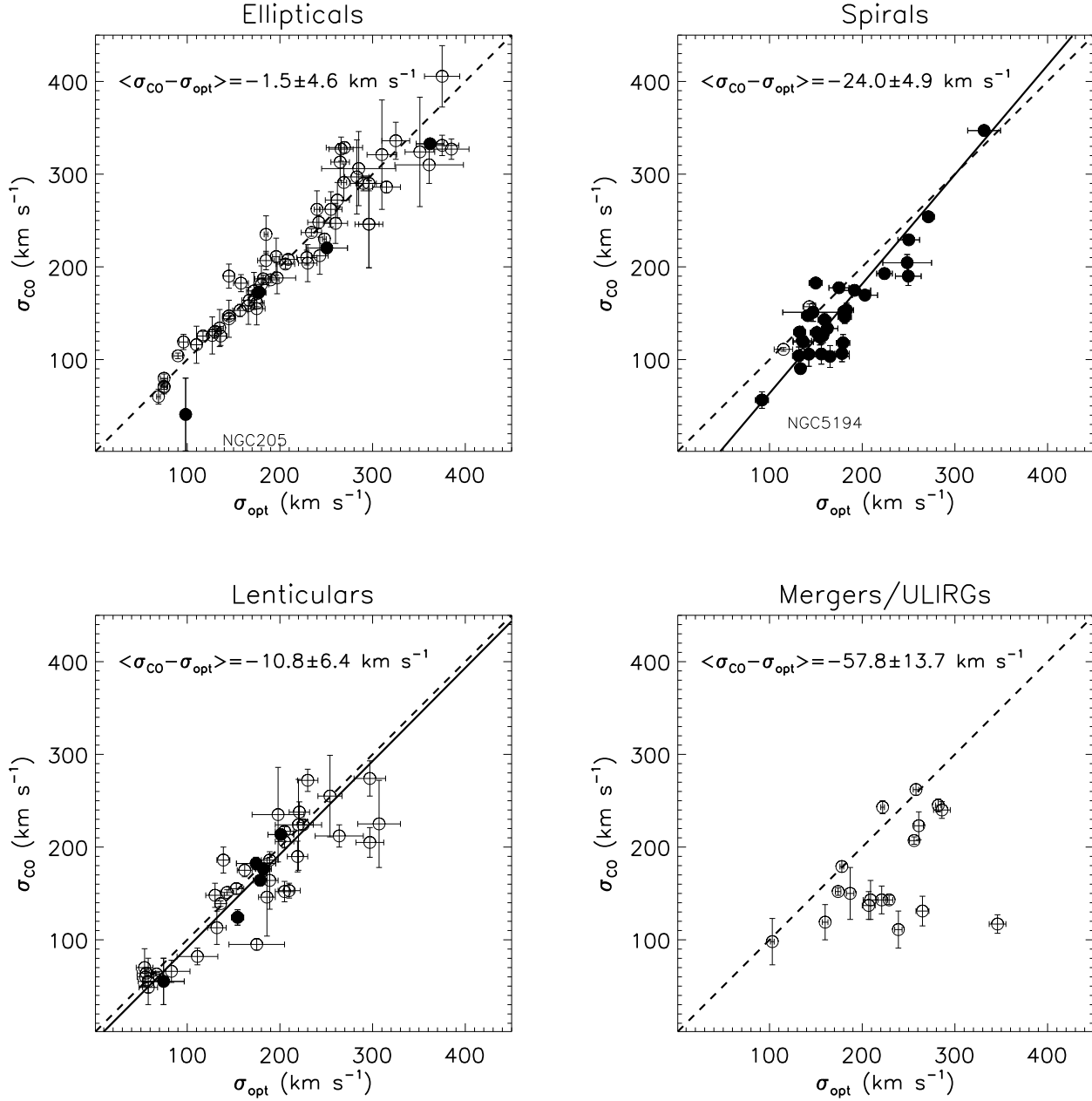


**Figure 4.** Comparison of the  $\sigma$  values in the near-IR with the optical values for distinct morphological types. The objects from our sample are shown as filled circles and open circles are for measurements from the literature. The dashed line shows a one-to-one relation and the continuous line is the best linear fit of the data. NGC 205 and NGC 5194, which have  $\sigma$  smaller than the instrumental resolution, are identified in the plots

value smaller than the spectral resolution of the data, we find the same relation, with  $\epsilon_{\langle\sigma_{\text{CO}}-\sigma_{\text{CaT}}\rangle} = 5.0 \text{ km s}^{-1}$ . Most objects have  $\sigma$  smaller than  $200 \text{ km s}^{-1}$  and for these objects  $\sigma_{\text{CO}}$  is clearly smaller than  $\sigma_{\text{opt}}$ .

The best linear equation for spiral galaxies is

$$\sigma_{\text{opt}} = (46.0 \pm 18.1) + (0.85 \pm 0.12)\sigma_{\text{CO}}, \quad (2)$$

where we excluded from the fit the galaxy NGC 5194 (identified in Fig. 4). The main cause of uncertainty in Eq. 2 is the small range of  $\sigma$  probed by the observations. Further observations are needed

to cover the high  $\sigma$  region ( $\sigma \gtrsim 220 \text{ km s}^{-1}$ ), and higher spectral resolution observations of objects with  $\sigma \lesssim 100 \text{ km s}^{-1}$ , in order to improve the calibration of the equation above.

We therefore observe that  $\sigma_{\text{CO}}$  and  $\sigma_{\text{opt}}$  become both more similar and more correlated in early-type galaxies compared with spirals and ULIRGs/merger remnants.



### 6.1 What is the origin of the sigma discrepancy for late-type galaxies?

As discussed above and in §1, the discrepancy between the stellar velocity dispersion obtained from optical bands and that obtained from the near-IR CO absorption band heads is larger for mergers of galaxies and ULIRGs than for early-type galaxies. Rothberg & Fischer (2010) found a correlation between the infrared luminosity ( $L_{\text{IR}}$ ) and  $\sigma_{\text{frac}}$  for merger remnants, while no correlation is found for elliptical galaxies. Rothberg et al. (2013) showed that the correlation found for merger remnants extends to ULIRGs, suggesting that dust might play an important role in the  $\sigma_{\text{CO}}$  values for this kind of object.

Figure 5 shows a plot of  $\sigma_{\text{frac}} = \frac{\sigma_{\text{CO}} - \sigma_{\text{opt}}}{\sigma_{\text{opt}}}$  vs.  $\log L_{\text{IR}}$  for the galaxies with available infrared luminosities (from Ho, Filippenko & Sargent (1997), Rothberg et al. (2013) and Rothberg & Fischer (2010)). The values of  $L_{\text{IR}}$  were estimated using their infrared fluxes  $F_{\text{IR}}$  from Ho, Filippenko & Sargent (1997), who defined it as  $F_{\text{IR}} = 1.26 \times 10^{-14} (2.58 S_{60} + S_{100}) \text{ W m}^2$ ,  $S_{60}$  and  $S_{100}$  being the flux densities at 60 and 100  $\mu\text{m}$ , respectively. Although data with higher angular resolution and wider wavelength coverage are now available from Herschel and Spitzer Telescopes, we use the IRAS fluxes since they are available for most of our objects, while Herschel and Spitzer data are still not available for most of them (e.g. Marleau et al. 2006; Sauvage et al. 2013; De Looze et al. 2012; Ciesla et al. 2012; Auld et al.). Figure 5 shows that galaxies with higher  $L_{\text{IR}}$  also have higher negative values of  $\sigma_{\text{frac}}$ , and that the spiral galaxies fill the gap between early-type objects and merger remnants. This smooth trend suggests that dust might play some role in the observed  $\sigma$ -discrepancy, as more warm dust is expected in spiral galaxies than in elliptical galaxies, and less than in merger remnants and ULIRGs.

Following Rothberg & Fischer (2010) we estimate the mass of dust by

$$\frac{M_{\text{dust}}}{M_{\odot}} = 0.959 S_{100} D^2 \left[ \left( 9.96 \frac{S_{100}}{S_{60}} \right)^{1.5} - 1 \right], \quad (3)$$

where  $S_{60}$  and  $S_{100}$  are the IRAS flux densities at 60 and 100  $\mu\text{m}$  in Jy, respectively, and  $D$  is the distance to the galaxy in Mpc (see also Hildebrand 1983; Thuan & Sauvage 1992). Rothberg & Fischer (2010) found that  $\sigma_{\text{frac}}$  correlates with  $M_{\text{dust}}$  for merger remnants, while no correlation is found for elliptical galaxies. Figure 6 shows the plot of  $\sigma_{\text{frac}}$  vs.  $M_{\text{dust}}$  for the galaxies studied here. A similar trend to that seen in Fig. 5 is observed in this plot, suggesting that dust plays a role in the observed  $\sigma$ -discrepancy for spirals and merger remnants.

Dust may be relevant to the  $\sigma$ -discrepancy in two ways. First, as extinction is lower in the K band, the  $\sigma_{\text{CO}}$  measurements could probe a dynamically cold, disk-like component that is more obscured than the dynamically hot bulge stars. Indeed, near-IR studies of nearby galaxies show that the reddening obtained from near-IR lines is larger than that obtained from optical lines, indicating that the near-IR samples an obscuring column larger than the optical spectral region (e.g. Moorwood & Oliva 1988; Heisler & De Robertis 1999; Martins et al. 2013a). Assuming a standard Galactic extinction curve (Weingartner & Draine 2001; Draine 2003), the extinction at 0.85  $\mu\text{m}$  (CaT) is about a factor of 5 larger than that at 2.3  $\mu\text{m}$  (CO), and the extinction at 0.52  $\mu\text{m}$  (Mgb) is about a factor of 2 greater again. If the difference between  $\sigma_{\text{CaT}}$  and  $\sigma_{\text{CO}}$  is due to extinction, we may also expect a difference between  $\sigma_{\text{CaT}}$  and  $\sigma_{\text{Mgb}}$ . However, Barth, Ho & Sargent

(2002a) compared  $\sigma_{\text{CaT}}$  and  $\sigma_{\text{Mgb}}$  and did not find any systematic difference between them.

Secondly, warm ( $T \sim 50 \text{ K}$ ), FIR-emitting dust may be associated with star formation in these galaxies. Indeed, the emission of the warm dust is directly correlated with the star formation rate, as it is heated by young stars (Kennicutt 1998; Kennicutt & Evans 2012).

Young stars form in disks, and in the absence of major perturbations generally remain dynamically cold. Indications of young stars in disks have been found in recent spatially resolved spectroscopy of galaxy nuclei with the Near-IR IFU Spectrograph (NIFS) on Gemini North. Riffel et al. (2010, 2011) and Storchi-Bergmann et al. (2012) carried out stellar population synthesis and found a spatial relation between low  $\sigma_{\text{CO}}$  and the young/intermediate age stellar population, confirming that  $\sigma_{\text{CO}}$  is affected by the presence of young/intermediate age stars. The presence of a young stellar population has also been proposed as an explanation of the  $\sigma$ -drop observed in some galaxies (e.g. Emsellem et al. 2001; Márquez et al. 2003). However, the comparison of our results with spatially resolved measurements should be taken with caution. While the NIFS data resolve a dynamically cold structure, our single-aperture measurements probe the second moment of the LOSVD, which does not necessarily imply a direct link between the two sets of results. New spatially resolved measurements of both the CaT and CO lines would show whether the effect we are observing here is related to the low- $\sigma$  regions observed in the works cited above.

If the difference between  $\sigma_{\text{CO}}$  and  $\sigma_{\text{CaT}}$  is due to the presence of a young stellar population in the disk of the galaxies, young stars must contribute more to the CO absorption features than do older stars, and the effect of this population on the  $\sigma$  measured from the CaT and optical lines must be negligible. The connection between the CO and CaT bands and the age of the stellar population is not straightforward, though. For example, the CO bands are relatively strong in both young/intermediate-age stars (AGB/TP-AGB stars) and old ones (M stars), while hotter, younger stars produce strong CaT bands along with weak CO features (e.g. Maraston 2005; Riffel et al. 2007). On the other hand, previous work has shown that  $\sigma_{\text{CaT}}$  is not very sensitive to the stellar population (Barth, Ho & Sargent 2002b,a). Full stellar population synthesis would help to resolve these issues, although different models currently make very different predictions for the NIR spectral region (e.g. Bruzual & Charlot 2003; Maraston 2005).

### 6.2 Implications for the $M_{\bullet}$ - $\sigma$ relationship

As discussed above, the  $\sigma$  discrepancy observed in our sample of mostly late-type galaxies does not appear in previous studies of early-type galaxies. We can use the measured  $\sigma$  values to evaluate the impact of the  $\sigma$  discrepancy on determinations of the mass of the central SMBH using the  $M_{\bullet}$  -  $\sigma$  relationship. Several studies have aimed at properly calibrating the  $M_{\bullet}$  -  $\sigma$  relation for distinct classes of objects. Xiao et al. (2011) investigated the  $M_{\bullet}$  -  $\sigma$  relation using a sample of 93 late-type galaxies with a Seyfert 1 nucleus. They found no difference in the slope for subsamples of barred and unbarred galaxies, but they found a small offset in the relation between low- and high-inclination disk galaxies, with the latter having a larger  $\sigma$  value for a given black hole mass. For a review of calibrations of the  $M_{\bullet}$  -  $\sigma$  relation, see Kormendy & Ho (2013).

Actually, Kormendy, Bender & Cornell (2011) show that the physically relevant parameter in black hole correlations with host

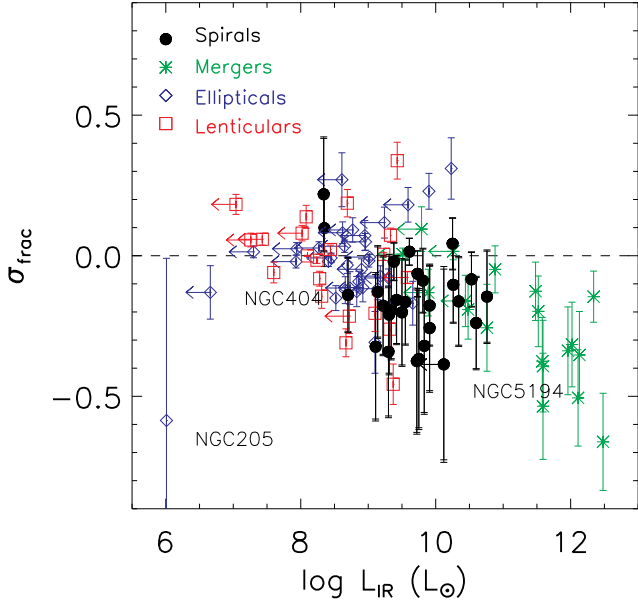


**Figure 5.** Fractional difference between  $\sigma_{\text{CO}}$  and  $\sigma_{\text{CaT}}$ ,  $\sigma_{\text{frac}} = \frac{\sigma_{\text{CO}} - \sigma_{\text{CaT}}}{\sigma_{\text{CaT}}}$  vs.  $L_{\text{IR}}$ . The three objects with  $\sigma$  values smaller than the spectral resolution of our data are identified in the plot.

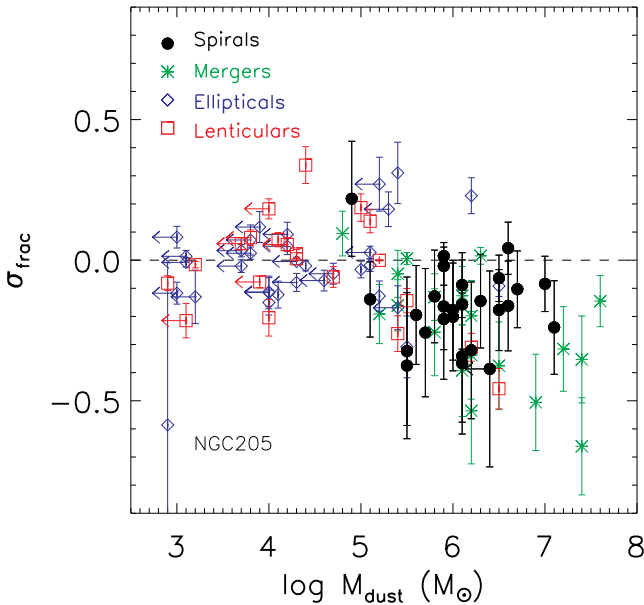


**Figure 6.**  $\sigma_{\text{frac}}$  vs.  $\log M_{\text{dust}}$  for distinct types of objects.

galaxy type is not early-type vs. late-type objects, but rather classical bulges versus pseudo bulges. The latter is defined as the buildup of dense central components that look like classical merger-built bulges but that were in fact formed slowly by disks out of disk material (Kormendy & Kennicutt 2004).

Since the aim of the present paper is to evaluate the impact of the use of CO-based measurements of the stellar velocity dispersion on the derived mass of the super-massive black hole, and not to

calibrate the  $M_{\bullet}$  –  $\sigma$  relationship, we use the same calibration for all objects of our sample, given by (Kormendy & Ho 2013) as:

$$\log \left( \frac{M_{\bullet}}{10^9 M_{\odot}} \right) = -(0.500 \pm 0.049) + (4.420 \pm 0.295) \log \left( \frac{\sigma}{200 \text{ km s}^{-1}} \right). \quad (4)$$

We estimated the mass of the SMBH for all spiral galaxies of our sample using  $\sigma_{\text{CaT}}$  and  $\sigma_{\text{CO}}$  in the equation above. The mean logarithmic difference is  $-0.29 \pm 0.12$ , which may be taken as a systematic error in the  $M_{\bullet}$  –  $\sigma$  relation when using CO-based estimates of the stellar velocity dispersion.

## 7 CONCLUSIONS

We have used  $0.85 - 2.5 \mu\text{m}$  spectroscopy of a sample of 48 galaxies (35 spirals, 7 lenticulars and 6 ellipticals) obtained with the Gemini Near-Infrared Spectrograph (GNIRS) on Gemini North telescope to measure the stellar kinematics by fitting the K-band CO absorption band heads and the CaT at  $8550 \text{ \AA}$ . This work is aimed at determining whether the difference in  $\sigma_{\text{CO}}$  and  $\sigma_{\text{CaT}}$  (the “ $\sigma$ – discrepancy”) reported for ULIRGs and merger remnants persists in the hitherto unexplored regime of late-type galaxies. Our main conclusions are:

- The velocity dispersion obtained from the  $2.29 \mu\text{m}$  CO bandheads is slightly smaller than the one from fitting the CaT, with an average difference of  $\sigma_{\text{CO}} - \sigma_{\text{CaT}} = -19 \pm 6 \text{ km s}^{-1}$  for the complete sample (all morphological types).
- We compiled the available  $\sigma$  values from literature and found an almost one-to-one relation between optical (CaT, Mgb, etc.) and CO-based estimates for early-type galaxies. For spiral galaxies the discrepancy is higher, but still much lower than for merger remnants. The best fit for spiral galaxies is  $\sigma_{\text{opt}} = (46.0 \pm 18.1) + (0.85 \pm 0.12)\sigma_{\text{CO}}$ , but more observations covering the  $\sigma$  ranges  $\sigma < 100 \text{ km s}^{-1}$  and  $\sigma > 200 \text{ km s}^{-1}$  are needed to properly calibrate this relation.
- The fractional  $\sigma$  difference correlates with the infrared luminosity, which may suggest that the  $\sigma$ -discrepancy is related to the presence of warm dust. In this scenario, the CO absorption band heads would be dominated by young stars located in the disc of the galaxy and thus result in smaller  $\sigma$  values, while the optical estimates are less sensitive to variations in the stellar population. However, the detailed spectral synthesis that would be needed to test this interpretation requires high spectral resolution SSP models, which are not yet available.

- We investigated the impact of the  $\sigma$ -discrepancy on the mass of the SMBH obtained via the  $M_{\bullet}$  –  $\sigma$  relation and found a mean logarithmic difference of  $-0.29 \pm 0.12$ , that must be considered as a systematic error in the SMBH mass when using  $\sigma_{\text{CO}}$  for spiral galaxies. However, this uncertainty is dominated by scatter of the relation and the conversion from  $\sigma_{\text{CO}}$  to  $\sigma_{\text{opt}}$  may introduce a even larger uncertainty in the derived  $M_{\bullet}$ .

Although the “ $\sigma$ – discrepancy” has already been discussed for ULIRGs and merger remnants (e.g. Rothberg & Fischer 2010; Rothberg et al. 2013) and no discrepancy was found for early-type galaxies (e.g. Silge & Gebhardt 2003; Vanderbeke et al. 2011; Kang et al. 2013), this is the first time that this comparison is done for a sample of mostly late-type galaxies.

## ACKNOWLEDGEMENTS

We thank an anonymous referee for useful suggestions which helped to improve the paper and S. Rembold for help with the bootstrap technique. This work is based on observations obtained at the Gemini Observatory, which is operated by the Association of Universities for Research in Astronomy, Inc., under a cooperative agreement with the NSF on behalf of the Gemini partnership: the National Science Foundation (United States), the Science and Technology Facilities Council (United Kingdom), the National Research Council (Canada), CONICYT (Chile), the Australian Research Council (Australia), Ministério da Ciência, Tecnologia e Inovação (Brazil) and Ministerio de Ciencia, Tecnología e Innovación Productiva (Argentina). *R.A.R.* acknowledges support from FAPERGS (project NO. 12/1209-6) and CNPq (project NO. 470090/2013-8). *L.C.H.* acknowledges support from the Kavli Foundation, Peking University, and grant NO. XDB09030102 (Emergence of Cosmological Structures) from the Strategic Priority Research Program of the Chinese Academy of Sciences. *A.R.A.* acknowledges CNPq for partial support to this work through grant 307403/2012-2. *L.M.* thanks CNPq through grant 305291/2012-2. *L.C.* acknowledges support from the Special Visiting Researcher Fellowship (PVE 313945/2013-6) under the Brazilian Scientific Mobility Program “Ciências sem Fronteiras”. *R.R.* acknowledges funding from FAPERGs (ARD 11/1758-5) and CNPq (PeP 304796/2011-5). *C.R.A.* is supported by a Marie Curie Intra European Fellowship within the 7th European Community Framework Programme (PIEF-GA-2012-327934) and by the Spanish Ministry of Science and Innovation (MICINN) through project PN AYA2010-21887-C04.04.

## REFERENCES

- Auld, R. et al., 2013, 428, 1880.  
 Barth, A. J., Ho, L. C., Sargent, W. L. W., 2002, ApJ, 124, 2607.  
 Barth, A. J., Ho, L. C., Sargent, W. L. W., 2002, ApJ, 566, L13.  
 Beers, T. C., Flynn, K., Gebhardt, K., 1990, AJ, 100, 32.  
 Bellovary, J., Holley-Bockelmann, K., Gültekin, K., Christensen, C., Governato, F., Brooks, A., Loebman, S., Munshi, F., 2014, <http://arxiv.org/abs/1405.0286>  
 Bender, R., Burstein, D., & Faber, S. M. 1993, ApJ, 411, 153  
 Bernardi, M. et al. 2003, AJ, 125, 1866.  
 Bourne, N. et al. 2013, MNRAS, 436, 479.  
 Bower, R. G. et al. 2006, MNRAS, 370, 645.  
 Bruzual, G., Charlot, S., 2003, MNRAS, 344, 1000.  
 Cappellari, M. & Emsellem, E., 2004, PASP, 116, 138.  
 Cappellari, M. et al., 2007, MNRAS, 379, 418.  
 Cenarro, A. J., Cardiel, N., Gorgas, J., Peletier, R. F., Vazdekis, A., Prada, F., 2001, MNRAS, 326, 959.  
 Cid Fernandes, R., Gu, Q., Melnick, J., Terlevich, E., Terlevich, R., Kunth, D., Rodrigues Lacerda, R., Joguet, B., 2004, MNRAS, 355, 273.  
 Ciesla, L. et al., 2012, A&A, 543, 161.  
 Cox, T. J., Dutta, S. N., Di Matteo, T., Hernquist, L., Hopkins, P. F., Robertson, B., Springel, V., 2006, ApJ, 650, 791.  
 Cushing, M.C., Rayner, J.T., & Vacca, W.D., 2005, ApJ, 623, 1115.  
 Davies J. I. et al., 2012, MNRAS, 419, 3505.  
 De Looze, I. et al., 2012, MNRAS, 423, 2359.  
 Di Matteo, T., Springel, V. & Hernquist, L. 2005, Nature, 433, 604.  
 Djorgovski, S., Davis, M., 1987, ApJ, 313, 59.  
 Draine, B. T., 2003, ARAA, 41, 241.  
 Dressler, A. 1984, ApJ, 281, 512  
 Dressler, A. 1984, ApJ, 286, 97  
 Dressler, A., Lynden-Bell, D., Burstein, D., Davies, R. L., Faber, S. M., Terlevich, R., Wegner, G., 1987, ApJ, 313, 42.  
 Emsellem, E., Greusard, D., Combes, F., Friedli, D., Leon, S., Pécontal, E., Wozniak, H., 2001, A&A, 368, 52.  
 Emsellem, E., Cappellari, M., Peletier, R. F., McDermid, R. M., Bacon, R., Bureau, M., Copin, Y., Davies, R. L., Krajnović, D., Kuntschner, H., Miller, B. W., & de Zeeuw, P. T. 2004, MNRAS, 352, 721.  
 Falcón-Barroso, J. Peletier, R. F., Balcells, M., 2002, MNRAS, 335, 741.  
 Ferrarese, L. & Ford, H. C., 2005, Space Science Reviews, 116, 523.  
 Ferrarese, L. & Merrit, D., 2000, ApJ, 547, 140.  
 Gebhardt, K., Richstone, D., Tremaine, S., Lauer, T. R., Bender, R., Bower, G., Dressler, A., Faber, S. M., Filippenko, A. V., Green, R., Grillmair, C., Ho, L. C., Kormendy, J., Magorrian, J., & Pinkney, J. 2003, ApJ, 583, 92  
 Gebhardt, K. et al. 2000, ApJ, 539, 13.  
 Graham, A. W., Onken, C. A., Athanassoula, E., Combes, F., 2011, MNRAS, 412, 2211.  
 Gültekin, K., Cackett, E. M., Miller, J. M., Di Matteo, T., Markoff, S., Richstone, D. O., 2008, ApJ, 706, 404.  
 Heisler C. A., De Robertis M. M., 1999, AJ, 118, 2038.  
 Ho, L. C., Filippenko, A. V., Sargent, W. L., 1995, ApJS, 98, 477.  
 Ho, L. C., Filippenko, A. V., Sargent, W. L., 1997, ApJS, 112, 31.  
 Ho, L. C., Greene, J. E., Filippenko, A. V., Sargent, W. L., 2009, ApJS, 183, 1.  
 Hildebrand, R. H. 1983, Q. J. R. Astron. Soc., 24, 267  
 Ivanov, V. D., Rieke, G. H., Groppi, C. E., Alonso-Herrero, A., Rieke, M. J., Engelbracht, C. W., 2000, ApJ, 545, 190.  
 Kang, W.-R., Woo, J.-H., Schulze, J., Riechers, D. A., Kim, S. C., Park, D., & Smolcic, V., 2013, ApJ, 767, 26.  
 Kennicutt R. C., 1998, ARA&A, 36, 189  
 Kennicutt R. C., Evans N. J., 2012, ARA&A, 50, 531.  
 Kormendy, J., & Kennicutt, R., ARA&A, 2004, 42, 603.  
 Kotilainen, J. K., Hyvönen, T., Reunanen, J., Ivanov, V. D., 2012, MNRAS, 425, 1057.  
 Kormendy, J. Bender, R., & Cornell, M. E., Nature, 2011, 469, 374.  
 Kormendy, J., & Ho, L. C. 2013, ARA&A, 51, 511.  
 Kuntschner, H., MNRAS, 2000, 315, 184.  
 Maraston, C., 2005, MNRAS, 362, 799.  
 Magorrian, J. et al. 1998, AJ, 115, 2285.  
 Nemmen R., Bower, R., Babul, A. & Storchi-Bergmann, T. 2007, MNRAS, 377, 1652  
 Marleau, F. R. et al., 2006, ApJ, 646, 929.  
 Martins, L. P., Rodríguez-Ardila, A., Diniz, S., Gruenwald, R., de Souza, R., 2013a, MNRAS, 431, 1823.  
 Martins, L. P., Rodríguez-Ardila, A., Diniz, S., Riffel, R., de Souza, R., 2013b, MNRAS, 435, 2861.  
 Márquez, I. Masegosa, J., Durret, F., González Delgado, R. M., Moles, M., Maza, J., Pérez, E., Roth, M., 2003, A&A, 409, 459.  
 Moorwood A. F. M., Oliva E., 1988, A&A, 203, 278  
 Naab, T. et al., 2013, arXiv:1311.0284  
 Origlià, L., Moorwood, A. F. M., Oliva, E., 1993, A&A, 280, 5360.  
 Rayner, J.T., Cushing, M.C., & Vacca, W.D., 2009, ApJS, 185, 289.

- Richstone, D. et al., 1998, *Nature*, 395, A14.
- Rothberg, B., & Fischer, J., 2010, *ApJ*, 712, 318.
- Rothberg, B., Fischer, J., Rodrigues, M., & Sanders, D. B., 2013, *ApJ*, 767, 72.
- Riffel, R., Rodríguez-Ardila, A., Pastoriza, M. G., 2006, *A&A*, 457, 61.
- Riffel, R., Pastoriza, M. G., Rodríguez-Ardila, A., Maraston, C., 2007, *ApJ*, 659L, 103.
- Riffel, Rogemar A., Storchi-Bergmann, T., Winge, C., McGregor, P. J., Beck, T., Schmitt, H., 2008, *MNRAS*, 385, 1129.
- Riffel, R., Pastoriza, M. G., Rodríguez-Ardila, A., Bonatto, C., 2009, *MNRAS*, 400, 273.
- Riffel, Rogemar A., 2010, *Ap&SS*, 327, 239.
- Riffel, Rogemar A. & Storchi-Bergmann, T., Riffel, R., & Pastoriza, M. G., 2010, *ApJ*, 713, 469.
- Riffel, R., Riffel, Rogemar A., Ferrari, F., Storchi-Bergmann, T., 2011, *MNRAS*, 416, 493.
- Sánchez-Blázquez, P., Peletier, R. F., Jiménez-Vicente, J., Cardiel, N., Cenarro, A. J., Falcón-Barroso, J., Gorgas, J., Selam, S., Vazdekis, A., 2006, *MNRAS*, 371, 703.
- Sauvage, M., et al. 2010, *A&A*, 518, 64.
- Silge, J. D., & Gebhardt, K., 2003, *ApJ*, 125, 2809.
- Silva, D. R., Kuntschner, H., Lyubenova, M., 2008, *ApJ*, 674, 194.
- Springel, V., Di Matteo, T. & Hernquist, L., 2005, *ApJ*, 620, 79.
- Storchi-Bergmann, T., Riffel, Rogemar A., Riffel, R., Diniz, M. R., Borges Vale, T., McGregor, P. J., 2012, *ApJ*, 755, 87.
- Terlevich, R., Davies, R. L., Faber, S. M., Burstein, D. 1981, *MNRAS*, 196, 381
- Tremaine, S. et al. 2002, *ApJ*, 574, 740.
- Thuan, T. X., & Sauvage, M. 1992, *A&AS*, 92, 749
- Valluri, M., Merritt, D., & Emsellem, E. 2004, *ApJ*, 602, 66.
- Vanderbeke, J., Baes, M., Romanowsky, A. J., & Schimidtobreck, L., 2011, *MNRAS*, 412, 2017.
- van der Marel, R. P., & Franx, M. 1993, *ApJ*, 407, 525.
- Weingartner, J.C., & Draine, B.T. 2001, *ApJ*, 548, 296.
- Winge, C., Riffel, Rogemar A., & Storchi-Bergmann, T., 2009, *ApJS*, 185, 186.
- Woo, J.-H., Schulze, A., Park, D., Kang, W.-R., Kim, S. C., & Riechers, D. A. 2013, *ApJ*, 772, 49
- Xiao, T., Barth, A. J., Greene, J. E., Ho, L. C., Bentz, M., C., Ludwig, R. R., & Jiang, Y., 2011, *ApJ*, 739, 28.

## APPENDIX A: FITS OF THE SPECTRA

Figures A1 and A2 show the resulting fit of the galaxy spectra for the CO and Ca triplet spectral regions, respectively.

## APPENDIX B: STELLAR TEMPLATES USED TO FIT THE STELLAR KINEMATICS

Table B1 shows the weights of each star (as well their spectral types) to the fit of the galaxy spectra for the CaT and CO spectral regions.

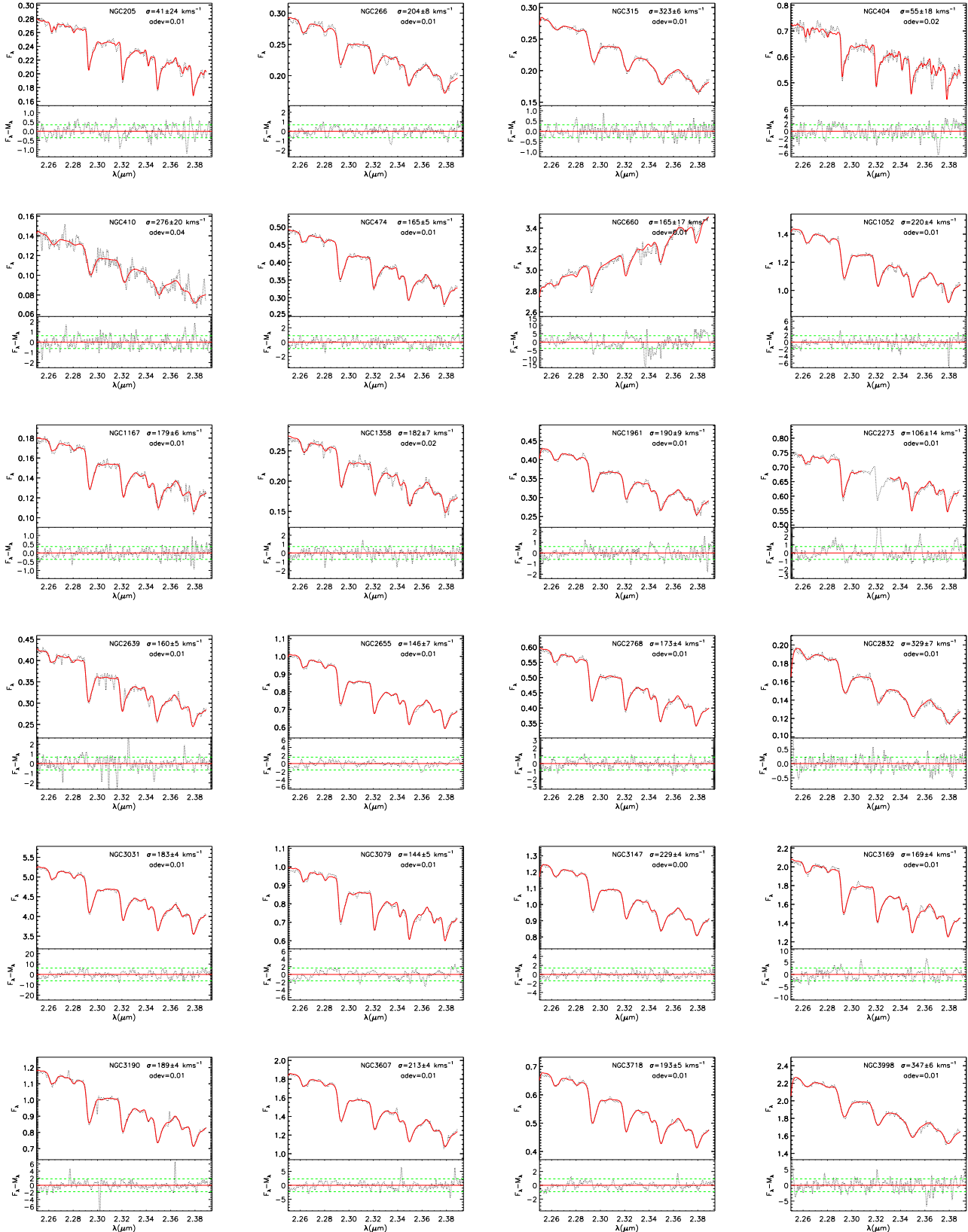


**Figure A1.** Fits of the CO absorption band-heads in the K band. The observed spectra are shown as dotted lines and the best-fit model as continuous lines. In the bottom panels the residuals of the fits (observed – model) are shown as dotted lines, where the dashed lines show the  $1 - \sigma$  level of the continuum. Fluxes are shown in units of  $10^{-15} \text{ erg s}^{-1} \text{ cm}^{-2} \text{ \AA}^{-1}$  and the residuals in units of  $10^{-17} \text{ erg s}^{-1} \text{ cm}^{-2} \text{ \AA}^{-1}$ . The *adev* parameter shown at each panel gives the percentage mean  $|OM|/O$  deviation over all fitted pixels, where *O* is the observed spectrum and *M* is the model.

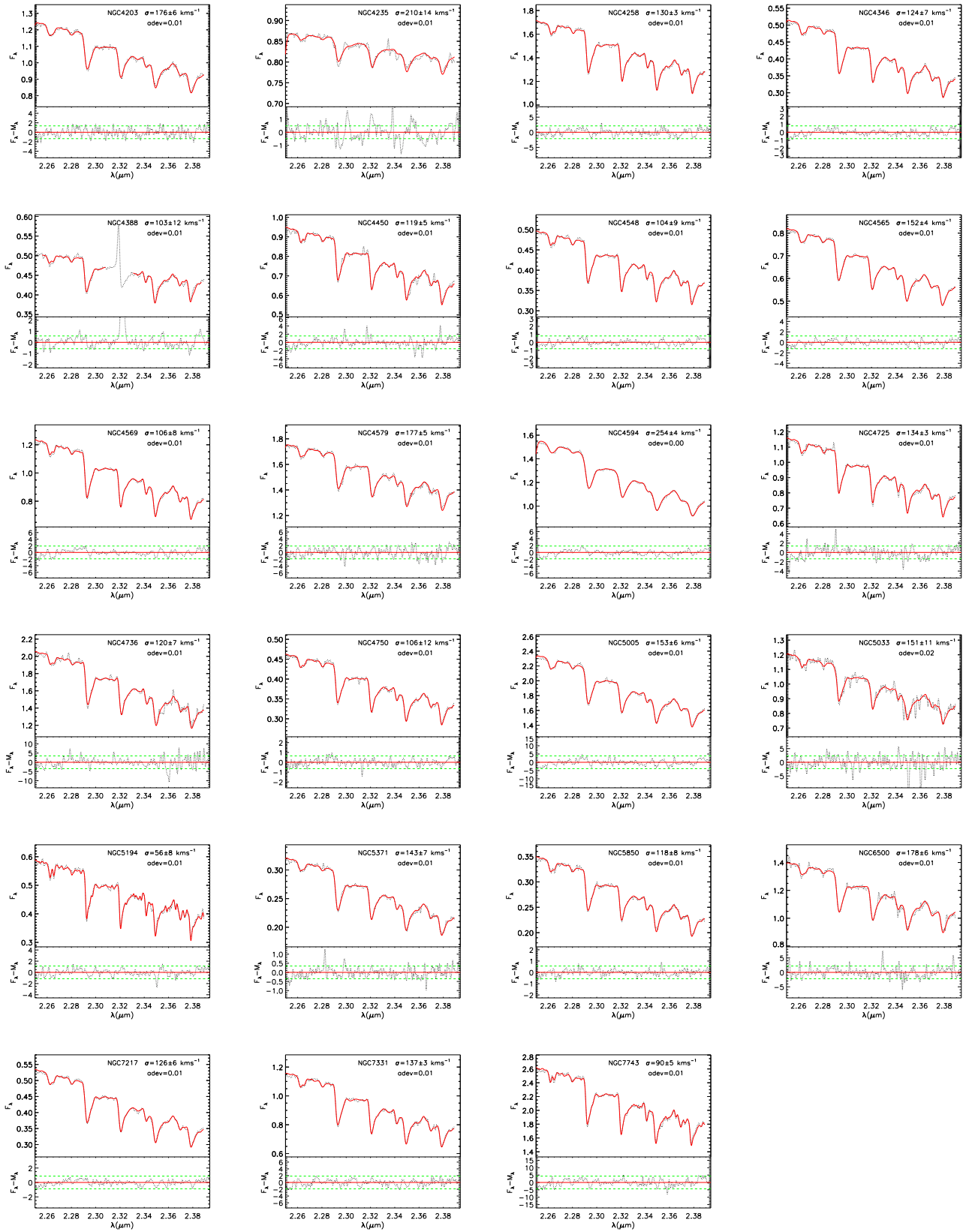


Figure A1. (continued)

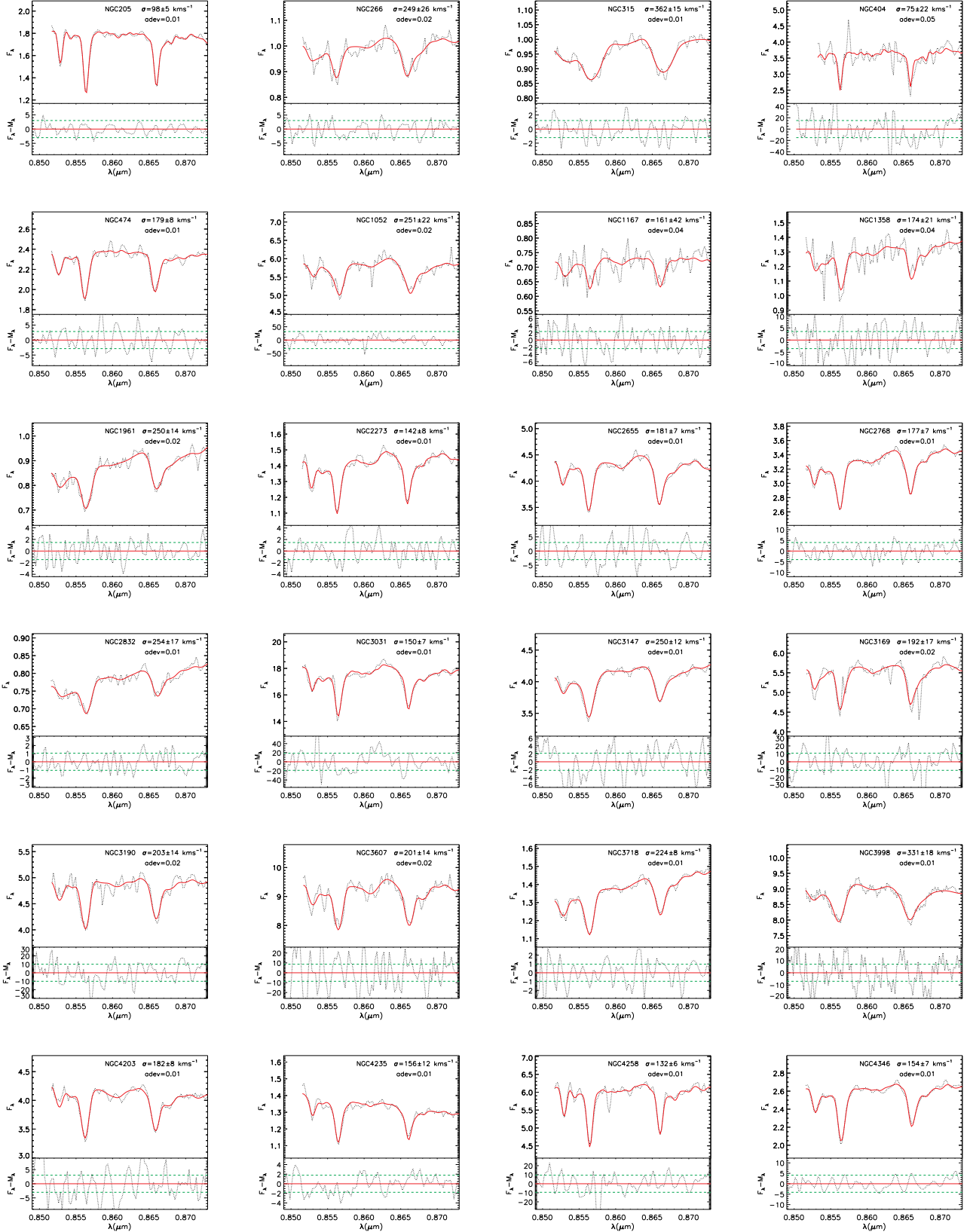


Figure A2. Same as Fig. A1 for the Ca triplet region.

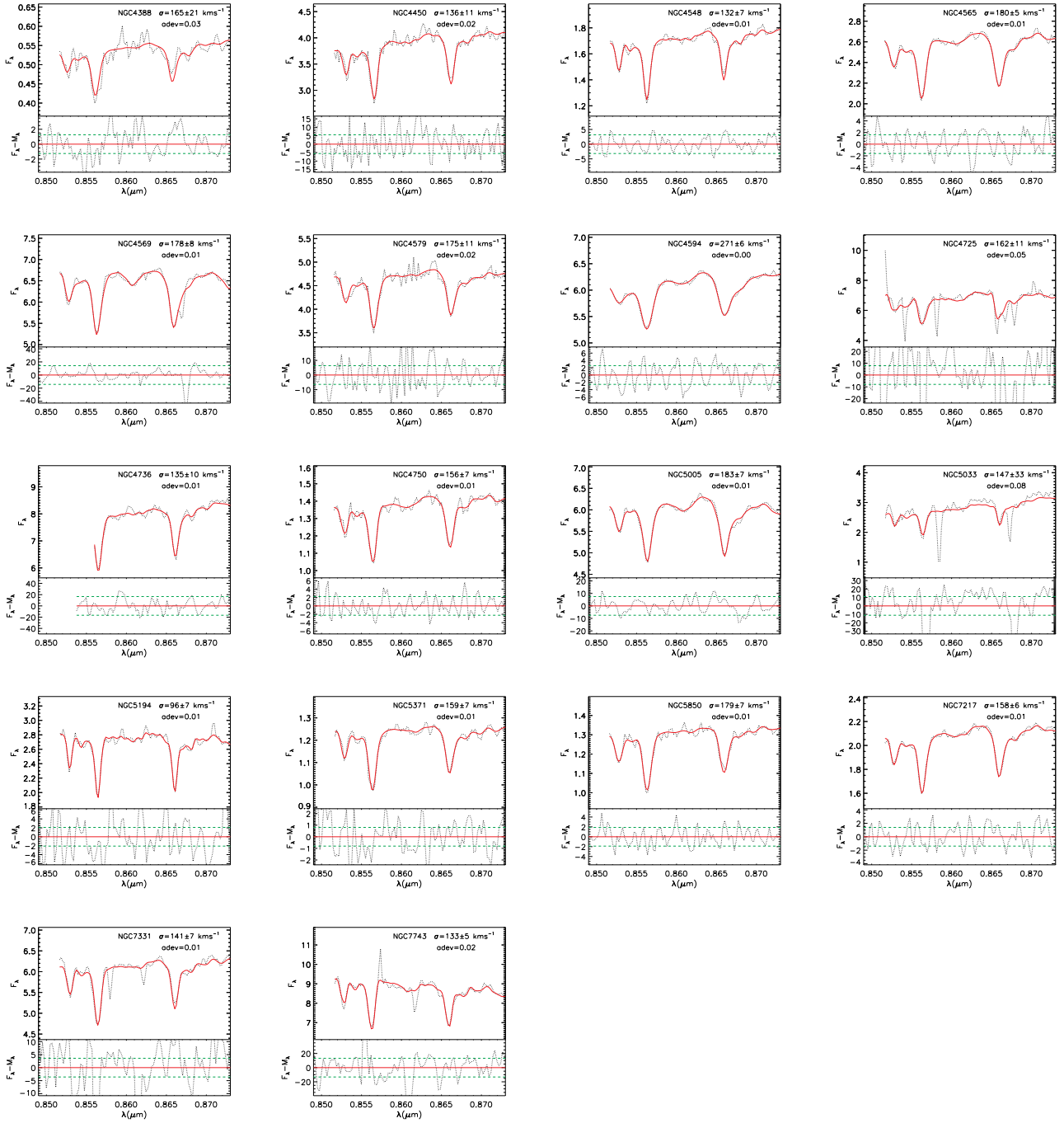


Figure A2. (continued)



**Table B1.** Stellar templates used for each galaxy to derive the stellar kinematics. Col 1: Galaxy name; Cols 2-4: Spectral and luminosity class, name and percentual contribution of the star to the fit of the galaxy spectrum for the Ca triplet region. Templates are from Cenarro et. al. (2001) and for some cluster stars, the authors list the positions of the stars in the HR diagram (SGB: subgiant branch; GB: giant branch; HB: horizontal branch). Cols 5-7: Same as Cols 2-4 for the CO spectral region. Templates are from Winge, Riffel & Storchi-Bergmann (2009).

Galaxy	CaT region			CO region		
	Spectral Type	Star	Weight (%)	Spectral Type	Star	Weight (%)
NGC205	F3III	HD115604	15	K0III	HD105028	7
	GB	M67-F-108	21	K2III	HD10598	5
	HB	M71-I-41	8	G8III	HD107467	16
	HB	M92-I-13	3	M3III	HD27796	7
	K0III	HD54810	37	M3III	HD112300	9
	K3III	HD58972	1	M0III	HD2490	12
	K4II	HD130705	3	K3III	HD4730	27
	K5III	HD139669	6	K7III	HD63425B	1
	K5III	HD149009	1	G3V	HD6461	11
M7.5III	HD126327	2				
NGC266	GB	M67-F-108	13	M3III	HD27796	6
	HB	M5-II-76	37	M2III	HD30354	38
	HB	M71-C	2	K8V	HD113538	41
	M5III	HD172816	45	M0III	HD2490	8
	M6III	HD148783	1	K7III	HD63425B	4
NGC315	GB	M67-F-108	33	M2III	HD30354	44
	GB	NGC188-II-122	29	G2Ib	HD209750	6
	HB	M5-II-53	4	M0III	HD2490	21
	K5III	HD149009	26	K0IV	HD34642	13
	M4III	HD17491	2	G5II	HD36079	13
	M7III	HD207076	3			
NGC404	GB	M67-F-108	26	K0III	HD105028	42
	HB	M5-II-76	34	K3Iab	HD339034	4
	HB	M92-XII-24	2	M0III	HD2490	42
	K5III	HD149009	21	K0IV	HD34642	10
	M7III	HD114961	15			
NGC410				M2III	HD30354	68
				K5II	HD3989	12
				K8V	HD113538	17
				K6III	HD32440	2
NGC474	F3III	HD115604	1	M3III	HD236791	1
	GB	NGC7789-501	25	M2III	HD30354	33
	HB	M92-I-13	19	K8V	HD113538	9
	K0III	HD54810	37	G2Ib	HD209750	3
	M6V	BD+19-5116-B	13	M0III	HD2490	29
	SGB	M67-IV-68	4	K6III	HD32440	17
				K0IV	HD34642	5
				K3Iab	HD339034	3
NGC660				G2Ib	HD209750	2
				K7III	HD63425B	15
				G8V	HD64606	80
NGC1052	HB	M5-II-53	5	M3III	HD236791	21
	HB	M92-I-13	19	M3III	HD27796	2
	K5III	HD139669	34	M2III	HD30354	4
	M7III	HD114961	18	K8V	HD113538	32
	SGB	M67-F-125	22	K7III	HD63425B	36
			G3V	HD6461	3	
NGC1167	F5VI	HD108177	47	M2III	HD30354	23
	G5III <sub>l</sub> we	HD88609	1	M2III	BD-01 3097	1
	GB	NGC188-II-122	35	K8V	HD113538	17
	HB	M92-XII-24	6	G2Ib	HD209750	4
	M7III	HD114961	8	M0III	HD2490	8
				K7III	HD63425B	43

**Table B1.** (continued)

Galaxy	CaT region			CO region		
	Spectral Type	Star	Weight (%)	Spectral Type	Star	Weight (%)
NGC1358	HB	M71-1-34	44	M2III	HD30354	57
	HB	M71-C	9	M2	BD+59 274	7
	K4III	HD149161	6	K8V	HD113538	33
	M5III	HD172816	24	M0III	HD2490	1
	M7III	HD114961	15			
NGC1961	GB	NGC188-I-57	27	M2III	HD30354	36
	K0V	HD149661	9	K8V	HD113538	24
	K5III	HD139669	39	M0III	HD2490	39
	M5.5III	HD94705	19			
	M6V	BD+19-5116-B	2			
	M7III	HD114961	1			
NGC2273	HB	M5-II-53	8	M2III	HD30354	18
	K4II	HD130705	39	K3lab	HD339034	1
	K5III	HD139669	1	K8V	HD113538	1
	M4III	HD17491	20	M0III	HD2490	19
	M5III	HD172816	8	K0IV	HD34642	4
	M5.5III	HD94705	1	G5II	HD36079	33
	M5III	HD175865	7	K7III	HD63425B	3
	SGB	M67-F-115	10	G8V	HD64606	11
	SGB	M67-F-125	5	G3V	HD6461	6
NGC2639				M2III	HD30354	42
				M3lab	BD+39 4208	11
				G2Ib	HD209750	29
				M0III	HD2490	16
NGC2655	F3III	HD115604	6	M2III	HD30354	7
	GB	M67-F-108	7	K3lab	HD339034	1
	HB	M5-II-53	8	K8V	HD113538	25
	K5III	HD139669	31	M0III	HD2490	40
	M6III	HD18191	22	K0IV	HD34642	1
	SGB	M67-F-125	24	K7III	HD63425B	23
NGC2768	GB	NGC188-I-85	8	M2III	HD30354	23
	HB	M71-1-41	16	K3lab	HD339034	1
	HB	M92-XII-24	4	K8V	HD113538	19
	K3III	HD102328	37	K1II	HD198700	3
	M6III	HD18191	24	M0III	HD2490	49
	SGB	M67-F-125	7	K0IV	HD34642	2
NGC2832	F0	BD-01-2582	1			1
	HB	M71-C	41	M2III	HD30354	30
	HB	M92-XII-24	2	K8V	HD113538	17
	M5.5III	HD94705	20	M0III	HD2490	51
	M6V	BD+19-5116-B	16			
	M7III	HD207076	6			
	SGB	M67-F-125	10			
NGC3031	GB	M67-F-231	1	M3III	HD27796	5
	GB	M92-XII-8	2	M2III	HD30354	14
	GB	NGC188-II-122	6	K8V	HD113538	21
	HB	M5-II-76	1	M0III	HD2490	10
	HB	M92-I-13	3	K0IV	HD34642	2
	K5III	HD139669	5	G5II	HD36079	8
	M5III	HD172816	25	K7III	HD63425B	25
	M7III	HD114961	18	G3V	HD6461	10
	SGB	M67-F-115	7	K4III	HD9138	1
	SGB	M67-IV-68	29			
	NGC 3079				M2III	HD30354
				K3lab	HD339034	2
				K8V	HD113538	18
				M0III	HD2490	39
				K7III	HD63425B	

Table B1. (continued)

Galaxy	CaT region			CO region		
	Spectral Type	Star	Weight (%)	Spectral Type	Star	Weight (%)
NGC3147	G2V	Hya-vB-64	2	M2III	HD30354	26
	GB	NGC188-I-61	8	K8V	HD113538	21
	HB	M71-C	1	G2Ib	HD209750	6
	K0III	HD88284	22	M0III	HD2490	5
	K4II	HD130705	46	K0IV	HD34642	1
	M6V	BD+19-5116-B	10	G5II	HD36079	7
	M7.5III	HD126327	4	K7III	HD63425B	31
	M7III	HD207076	3			
NGC3169	F2II	HD164136	15	M3III	HD27796	6
	GB	M67-F-108	19	M2III	HD30354	33
	GB	NGC7789-501	25	K3Iab	HD339034	4
	HB	M5-II-76	14	K8V	HD113538	6
	HB	M92-XII-24	7	G2Ib	HD209750	5
	M8III	HD113285	4	M0III	HD2490	28
	SGB	NGC188-I-88	12	K0IV	HD34642	4
				G3V	HD6461	9
NGC3190	F0V	Hya-vB-103	3	M2III	HD30354	14
	F6V	HD30652	1	K3Iab	HD339034	5
	GB	M67-F-108	8	K8V	HD113538	23
	HB	M71-1-41	32	M0III	HD2490	24
	K3III	HD169191	20	K7III	HD63425B	31
	M7III	HD207076	16			
	SGB	M67-F-125	17			
NGC3607	HB	M5-II-53	7	M2III	HD30354	36
	HB	M92-I-13	6	K8V	HD113538	20
	K0V	Coma-A-13	21	M0III	HD2490	42
	K5III	HD136028	4			
	K7V	HD157881	10			
	M4III	HD17491	27			
	M7III	HD114961	10			
	SGB	M67-F-125	12			
NGC3718	GB	M67-F-108	2			1
	GB	M71-1-71	1	M2III	HD30354	25
	HB	M71-C	14	K3Iab	HD339034	1
	K0III	HD63352	6	K8V	HD113538	22
	K5III	HD136028	13	M0III	HD2490	33
	M5III	HD175865	13	K7III	HD63425B	14
	SGB	M67-F-125	37	G3V	HD6461	2
	SGB	NGC188-I-97	11			
NGC3998	HB	M71-1-41	3	M2III	HD30354	20
	HB	M71-C	18	K8V	HD113538	10
	HB	M92-XII-24	9	K0IV	HD34642	29
	K0V	Coma-A-13	37	K7III	HD63425B	31
	K5III	HD136028	31	G3V	HD6461	7
NGC4203	GB	NGC188-I-61	30	M2III	HD30354	17
	HB	M5-II-53	4	M3Iab	BD+39 4208	2
	HB	M71-1-41	27	K8V	HD113538	24
	K0V	Coma-A-13	4	G2Ib	HD209750	5
	K5III	HD139669	4	G5II	HD36079	14
	K5III	HD149009	8	K7III	HD63425B	33
	K7V	HD157881	1	G8V	HD64606	2
	M7III	HD114961	19			
NGC4235	M1.5Vb	HD72905	55	G5II	HD36079	77
	G5III	HD134063	14	K7III	HD63425B	14
	K4III	HD131918	2	G3V	HD6461	7
	M7III	HD207076	15			
	SGB	M67-IV-68	11			

**Table B1.** (continued)

Galaxy	CaT region			CO region		
	Spectral Type	Star	Weight (%)	Spectral Type	Star	Weight (%)
NGC4258	G5IIIwe	HD2665	3	M3III	HD236791	5
	GB	NGC188-II-187	1	M3III	HD27796	4
	K1III	HD185644	62	M2III	HD30354	10
	K3III	HD169191	10	K3Iab	HD339034	2
	M7III	HD207076	18	K8V	HD113538	10
	SGB	M67-F-125	3	M0III	HD2490	10
				K0IV	HD34642	7
				K7III	HD63425B	25
				G8V	HD64606	1
				G3V	HD6461	21
NGC4346	G9III	HD112989	9	M2III	HD30354	32
	GB	NGC188-II-122	1	K8V	HD113538	19
	HB	M71-C	21	M0III	HD2490	25
	K3III	HD102328	37	K7III	HD63425B	22
	M4III	HD17491	13			
	SGB	M67-F-125	8			
	SGB	NGC188-I-97	8			
NGC4388	GB	M67-F-108	4	M2III	HD30354	23
	K7V	HD157881	46	K8V	HD113538	4
	M1III	HD168720	19	G5II	HD36079	13
	M6V	BD+19-5116-B	1	G8V	HD64606	15
	SGB	M67-F-115	27	G3V	HD6461	29
	SGB	M67-IV-68	1	K4III	HD9138	12
NGC4450	GB	NGC188-II-122	13	M2III	HD30354	29
	HB	M92-XII-24	7	K8V	HD113538	19
	K5III	HD120933	1	K1II	HD198700	14
	K5III	HD139669	42	M0III	HD2490	4
	M5V	Gl-699	16	K7III	HD63425B	22
	SGB	M67-F-115	15	G3V	HD6461	9
	SGB	NGC188-II-93	2			
NGC4548	HB	M71-C	16	M2III	HD30354	21
	HB	NGC188-I-105	4	K8V	HD113538	15
	K3III	HD102328	46	M0III	HD2490	28
	M5.5III	HD94705	10	K7III	HD63425B	12
	SGB	M67-F-125	4	G8V	HD64606	21
	SGB	NGC188-I-97	16			
NGC4565	GB	M67-F-108	16	M2III	HD30354	29
	GB	NGC188-I-57	3	K8V	HD113538	17
	HB	M71-1-41	7	G2Ib	HD209750	4
	HB	M92-XII-24	6	M0III	HD2490	39
	K0III	HD85503	11	K7III	HD63425B	4
	K5III	HD139669	17	G8V	HD64606	4
	M4III	HD17491	22			
	M7III	HD114961	4			
	SGB	M67-F-125	8			
NGC4569	F3III	HD115604	26	M2III	HD30354	21
	GB	M67-F-108	29	M3Iab	BD+39 4208	1
	GB	NGC188-I-75	1	K3Iab	HD339034	4
	HB	M71-1-41	18	K8V	HD113538	11
	HB	M92-XII-24	7	M0III	HD2490	59
	K5III	HD139669	9			
	M7III	HD114961	9			
NGC4579	F3III	HD115604	2	M2III	HD30354	16
	GB	NGC188-II-122	1	G2Ib	HD209750	1
	GB	NGC7789-971	8	M0III	HD2490	35
	HB	M92-XII-24	4	K7III	HD63425B	4
	K0III	HD142091	65	G8V	HD64606	42
	K5III	HD136028	6			
	SGB	M67-F-125	11			

Table B1. (continued)

Galaxy	CaT region			CO region		
	Spectral Type	Star	Weight (%)	Spectral Type	Star	Weight (%)
NGC4594	HB	M71-C	7	M2III	HD30354	27
	HB	M92-XII-24	2	K8V	HD113538	19
	K0V	Coma-A-13	36	M0III	HD2490	43
	K2III	HD54719	8	K7III	HD63425B	9
	K3III	HD102328	2			
	M4III	HD17491	3			
	M5III	HD172816	25			
	SGB	M67-F-125	14			
NGC4725	GB	M67-F-108	24	M2III	HD30354	19
	GB	NGC7789-971	2	K8V	HD113538	19
	HB	M5-II-53	11	G2Ib	HD209750	3
	M5III	HD172816	59	M0III	HD2490	34
	M7III	HD114961	1	K7III	HD63425B	21
				G3V	HD6461	2
NGC4736	F5	HD14938	2	M2III	HD30354	28
	G2V	HD76932	12	G2Ib	HD209750	17
	GB	M67-F-108	38	M0III	HD2490	53
	GB	NGC7789-971	8			
	HB	M5-II-53	3			
	HB	M92-I-13	10			
	K0III	HD63352	24			
NGC4750	HB	M92-XII-24	3	M2III	HD30354	22
	HB	NGC7789-676	4	K3Iab	HD339034	2
	K3III	HD102328	6	K8V	HD113538	15
	K4II	HD130705	14	G2Ib	HD209750	21
	K5III	HD149009	9	M0III	HD2490	8
	M4III	HD17491	16	K7III	HD63425B	28
	M5.5III	HD94705	7			
	SGB	M67-F-115	6			
	SGB	M67-F-125	13			
	SGB.	NGC188-I-55	16			
NGC5005	HB	M5-II-53	10	M2III	HD30354	20
	HB	M92-XII-24	4	K8V	HD113538	24
	K0V	Coma-A-13	9	M0III	HD2490	55
	K5III	HD139669	46			
	M5III	HD172816	3			
	SGB	M67-F-125	24			
NGC5033	GB	M67-F-108	64	M2III	HD30354	39
	HB	M5-II-53	7	K8V	HD113538	14
	M5.5III	HD94705	18	M0III	HD2490	29
	M7III	HD114961	9	G8V	HD64606	16
NGC5194	F3III	HD115604	2	M2III	HD30354	27
	GB	M67-F-108	33	M2III	BD-01 3097	13
	HB	M92-XII-24	7	K8V	HD113538	8
	K3III	HD102328	2	G2Ib	HD209750	15
	K4II	HD130705	5	M0III	HD2490	34
	K5III	HD139669	10			
	M4III	HD17491	25			
	SGB	M67-F-125	8			
	SGB	M67-IV-68	2			
NGC5371	F8V	Hya-vB-19	8	M2III	HD30354	38
	G2V	Hya-vB-64	18	K3Iab	HD339034	4
	HB	M71-C	4	K8V	HD113538	4
	K0III	HD88284	30	K1II	HD198700	1
	K4II	HD130705	19	G2Ib	HD209750	14
	M6V	BD+19-5116-B	9	hd218594	HD218594	2
	M7.5III	HD126327	9	M0III	HD2490	11
				K0IV	HD34642	2
				K7III	HD63425B	16

**Table B1.** (continued)

Galaxy	CaT region			CO region		
	Spectral Type	Star	Weight (%)	Spectral Type	Star	Weight (%)
NGC5850	F0V	HD112412	1	M2III	HD30354	30
	G2V	HD76932	10	K3Iab	HD339034	1
	F7V	HD102634	2	K8V	HD113538	19
	F8V	HD187691	1	G2Ib	HD209750	2
	GB	M92-XII-8	10	M0III	HD2490	33
	K0III	HD88284	36	K0IV	HD34642	1
	K3III	HD169191	1	K7III	HD63425B	10
	K4II	HD130705	22			
	M1III	HD168720	12			
M7.5III	HD126327	1				
NGC6500				M2III	HD30354	23
				K8V	HD113538	11
				G2Ib	HD209750	18
				K7III	HD63425B	48
NGC7217	F3III	HD115604	8	M2III	HD30354	34
	GB	NGC188-II-122	1	K3Iab	HD339034	1
	HB	M92-XII-24	2	K8V	HD113538	21
	K0V	Coma-A-13	11	M0III	HD2490	42
	K3III	HD102328	52			
	M4III	HD17491	10			
	M5III	HD175865	6			
M6V	BD+19-5116-B	6				
NGC7331	F6V	HD30652	1	M2III	HD30354	16
	G2V	Hya-vB-64	10	K8V	HD113538	19
	G5IIIwe	HD88609	12	M0III	HD2490	37
	G8III	HD38751	36	K7III	HD63425B	26
	HB	M71-C	9			
	K3III	HD102328	11			
M7III	HD207076	16				
NGC7743	HB	M71-C	34	M2III	HD30354	6
	HB	M92-XII-24	16	K3Iab	HD339034	4
	K0III	HD85503	41	K8V	HD113538	3
	M7III	HD114961	4	G2Ib	HD209750	5
	SGB	M67-F-125	2	M0III	HD2490	65
				K0IV	HD34642	12
			G3V	HD6461	2	